PNAS
www.pnas.org

Supplementary Information for:

Aerosol-photolysis interaction reduces particulate matter during wintertime haze events

Jiarui Wu, Naifang Bei, Bo Hu, Suixin Liu, Yuan Wang, Zhenxing Shen, Xia Li, Lang Liu, Ruonan Wang, Zirui Liu, Junji Cao, Xuexi Tie, Luisa T. Molina, and Guohui Li

Corresponding author: Guohui Li

Email: ligh@ieecas.cn

This PDF file includes:

Supplementary text

Figs. S1 to S24

Tables S1 to S3

SI References

www.pnas.org/cgi/doi/10.1073/pnas.1916775117

Supplementary Information Text

SI-1 WRF-Chem model and configurations

SI-1.1 WRF-Chem model

The WRF-Chem model (Version 3.5) (1) with modifications by Li et al. (2-4) has been applied to quantitatively evaluate the $PM_{2.5}$ contribution of the combination of ARI and API during a persistent heavy haze episode in the NCP. The model includes a new flexible gas phase chemical module and the CMAQ aerosol module developed by US EPA (5). For the aerosol simulations, the CMAQ/models-3 aerosol module (AERO5) has been incorporated into the model. In this aerosol component, the particle size distribution is represented as the superposition of three lognormal sub-distributions, called modes. The processes of coagulation, particles growth by the addition of mass, and new particle formation are included. The new particle production rate due to binary nucleation of H_2SO_4 and water vapor is parameterized following Kulmala et al. (6). The wet deposition is based on the method in the CMAQ module and the dry deposition of chemical species followed Wesely (7). The photolysis rates are calculated using the Fast Tropospheric Ultraviolet and Visible (FTUV) Radiation Model with the aerosol and cloud effects on photolysis (3, 8).

ISORROPIA (version 1.7) is used to predict the thermodynamic equilibrium between the ammonia-sulfate-nitrate-chloride-water aerosols and their gas phase precursors of H_2SO_4-HNO_3-NH_3-HCl-water vapor (9). The organic aerosol (OA) module is based on the volatility basis-set (VBS) approach with aging; detailed information can be found in Li et al. (4). The primary OA (POA) components from traffic-related combustion and biomass burning emissions are represented by nine surrogate species with saturation concentrations (C*) ranging from 10^{-2} to 10^{6} μg m^{-3} at room temperature (10), and assumed to be semi-volatile and photochemically reactive (11). The secondary OA (SOA) formation from each anthropogenic or biogenic precursor is calculated using four semi-volatile VOCs with

effective saturation concentrations of 1, 10, 100, and 1000 μg m^{-3} at 298 K. The SOA formation via the heterogeneous reaction of glyoxal and methylglyoxal is parameterized as a first-order irreversible uptake by aerosol particles and cloud droplets with an uptake coefficient of 3.7×10^{-3} (12-14).

SI-1.2 Model configurations

In the Base scenario simulation, the physical parameterizations include the microphysics scheme of Hong et al. (15), the Mellor, Yamada, and Janjić (MYJ) turbulent kinetic energy (TKE) planetary boundary layer scheme (16), the Unified Noah land-surface model (17), the Goddard longwave radiation scheme (18) and the Goddard shortwave parameterization (19). The NCEP 1° × 1° reanalysis data are used to obtain the meteorological initial and boundary conditions. The chemical initial and boundary conditions are interpolated from the 6h output of MOZART (20). The spin-up time of the WRF-Chem model is 4 days and 4 hours. The SAPRC-99 (Statewide Air Pollution Research Center, version 1999) chemical mechanism is used in the present study. The anthropogenic emissions are developed by Zhang et al. (21) and Li et al. (22), including contributions from agriculture, industry, power generation, residential, and transportation sources. The biogenic emissions are calculated online using the MEGAN (Model of Emissions of Gases and Aerosol from Nature) model developed by Guenther et al. (23). The Fire Inventory from NCAR (FINN) (24, 25) is taken for the biomass burning emissions in simulations. The model simulation domain is shown in Fig. S1a and detailed model configuration can be found in Table S1.

SI-1.3 Aerosol radiative module

In the present study, Goddard shortwave module developed by Chou and Suarez (18, 19) is employed to account for the ARI effect on particulate matter (PM) pollution and the FTUV module (3, 8) is used to consider the API effect. The aerosol radiative module developed by Li et al. (3) has been incorporated into the WRF-Chem model to calculate the aerosol optical

depth (AOD or $\boldsymbol{\tau_a}$), single scattering albedo (SSA or $\boldsymbol{\omega_a}$), and the asymmetry factor ($\boldsymbol{g_a}$).

In the CMAQ aerosol module, aerosols are represented by a three-moment approach with a lognormal size distribution:

$$\boldsymbol{n(lnD)} = \frac{N}{\sqrt{2\pi} ln\sigma_g} \boldsymbol{exp}[-\frac{1}{2}(\frac{lnD - lnD_g}{ln\sigma_g})^2] \quad (1)$$

Where D is the particle diameter, N is the number distribution of all particles in the distribution, D_g is the geometric mean diameter, and σ_g is the geometric standard deviation. To calculate the aerosol optical properties, the aerosol spectrum is first divided into 48 bins from 0.002 to 10.0 μm, with radius r_i. The aerosols are classified into four types: (1) internally mixed sulfate, nitrate, ammonium, hydrophilic organics and black carbon (BC), and water; (2) hydrophobic organics; (3) hydrophobic BC; and (4) other unidentified aerosols (generally dust-like aerosols). These four kinds of aerosols are assumed to be mixed externally. For the internally mixed aerosols, the complex refractive index at a certain wavelength (λ) is calculated based on the volume-weighted average of the individual refractive index. Given the particle size and complex refractive index, the extinction efficiency (Q_e), ω_a and g_a are calculated using the Mie theory at a certain wavelength (λ). The look-up tables of Q_e, ω_a and g_a are established according to particle sizes and refractive indices to avoid multiple Mie scattering calculation. The aerosol optical parameters are interpolated linearly from the look-up tables with the calculated refractive index and particle size in the module.

The $\boldsymbol{\tau_a}$ at a certain $\boldsymbol{\lambda}$ in a given atmospheric layer $\boldsymbol{k}$ is determined by the summation over all types of aerosols and all bins:

$$\boldsymbol{\tau_a(\lambda, k)} = \sum_{i=1}^{48} \sum_{j=1}^{4} \boldsymbol{Q_e}\,(\boldsymbol{\lambda, r_i, j, k})\boldsymbol{\pi r_i^2 n(r_i, j, k)\Delta Z_k} \quad (2)$$

where $\boldsymbol{n(r_i, j, k)}$ is the number concentration of $\boldsymbol{j}$-th kind of aerosols in the $\boldsymbol{i}$-th bin. $\boldsymbol{\Delta Z_k}$ is the depth of an atmospheric layer. The weighted-mean values of $\boldsymbol{\omega_a}$ and $\boldsymbol{g_a}$ are then calculated by using d'Almeida et al. (26):

$$\omega_a(\lambda,k) = \frac{\sum_{i=1}^{48}\sum_{j=1}^{4} Q_e(\lambda,r_i,j,k)\pi {r_i}^2 n(r_i,j,k)\omega_a(r_i,\mathrm{j},\mathrm{k})\Delta Z_k}{\sum_{i=1}^{48}\sum_{j=1}^{4} Q_e(\lambda,r_i,j,k)\pi {r_i}^2 n(r_i,j,k)\Delta Z_k} \quad (3)$$

$$g_a(\lambda,k) = \frac{\sum_{i=1}^{48}\sum_{j=1}^{4} Q_e(\lambda,r_i,j,k)\pi {r_i}^2 n(r_i,j,k)\omega_a(r_i,\mathrm{j},\mathrm{k})g_a(\lambda,r_i,\mathrm{j},\mathrm{k})\Delta Z_k}{\sum_{i=1}^{48}\sum_{j=1}^{4} Q_e(\lambda,r_i,j,k)\pi {r_i}^2 n(r_i,j,k)\omega_a(r_i,\mathrm{j},\mathrm{k})\Delta Z_k} \quad (4)$$

When the wavelength-dependent τ_a, ω_a, and g_a are calculated, they can be used in the Goddard shortwave module to evaluate the ARI effect and the FTUV to evaluate the API effect. The aerosol refractive indices used for Mie scattering calculation are listed in Table S2. In the base case simulation of the Base scenario, the BC aging from the hydrophobic to the hydrophilic state occurs at a pseudo first order rate of 9.26×10^{-5} s^{-1} (27) during daytime and 7.10×10^{-6} s^{-1} (28) during nighttime. As suggested by Moffet and Prather (27), the effective density is 0.7 g cm^{-3} for fresh BC and 1.8 g cm^{-3} for aged BC to consider the variation of the BC morphology. In order to take into account absorption of brown carbon (BrC) observed by Barnard et al. (29) in Megacities, the imaginary refractive index of POA measured by Kirchstetter et al. (30) is employed in the present study (Table S2). Detailed information can be found in Li et al. (3).

SI-1.4 Aerosol-cloud interactions module

A two-moment bulk microphysics scheme with aerosol effects developed by Li et al. (31) is utilized to account for aerosol-cloud interaction (ACI) in the simulation. The mass mixing ratio and number concentration of five hydrometeors are predicted in the bulk microphysics scheme, including cloud water, rain water, ice crystal, snow flake, and graupel. The Gamma function is used to represent the size distribution of the five hydrometeors. Detailed information is provided in Li et al. (31).

The aerosol activation to cloud condensation nuclei (CCN) and ice nuclei (IN) is based on the CMAQ/models3 aerosol module (5). Aerosols are simulated in the CMAQ using a modal approach assuming that particles are represented by three superimposed log-normal

size distributions. The aerosol species, including sulfate, nitrate, ammonium, POA, SOA, BC, and other unidentified species (dust-like) are predicted in the module.

For the CCN nucleation, the critical radius of dry aerosols is calculated from the *k*-Köhler theory developed by Petters and Kreidenweis (32-34) using water vapor supersaturation predicted by the model (35, 36). If the activated CCN radius is less than 0.03 μm, the mass of water condensation on CCN is calculated under the equilibrium assumption; otherwise, the mass of water condensing on CCN is calculated by $\boldsymbol{m_w = K\frac{4}{3}\pi r_a^3 \rho_w}$ at zero supersaturation, where $3 < K < 8$ (37). Additionally, a novel, flexible approach, proposed by Philips et al. (38, 39) is used to parameterize the ice heterogeneous nucleation within clouds. The method has empirically derived dependencies on the chemistry and surface area of multiple species of IN aerosols, mainly including dust, black and organic carbon aerosols. Three kinds of ice nucleation mechanisms are considered in the method, including contact, immersion, and condensation freezing. Detailed information can be found in Zhou et al. (40).

SI-2 Data and methodology

SI-2.1 Data description

The model performance is validated using the available measurements in the NCP, including AOD, SSA, cloud fraction (CF), cloud optical thickness (COT), planetary boundary layer height (PBLH), downward shortwave flux (SWDOWN), ultraviolet (UV) radiation reaching the surface (UVDOWN), aerosol species, and air pollutants. The daily AOD, CF, and COT are retrieved from Terra- and Aqua- Moderate Resolution Imaging Spectroradiometer (MODIS) level 2 products. The hourly SSA at 520nm is calculated using the measurement of the turbidity meter at the National Center for Nanoscience and Technology (NCNST), Chinese Academy of Sciences (116.33°E, 39.99°N) in Beijing (Fig. S1b). The daily PBLH at 12:00 Beijing time (BJT) is diagnosed from the radiosonde

observation at a meteorological site (116.47°E, 39.81°N) in Beijing. The hourly measurements of O_3, NO_2, SO_2, CO and $PM_{2.5}$ concentrations have been released by the Ministry of Ecology and Environment of China since 2013. The hourly submicron sulfate, nitrate, ammonium, and organic aerosols are measured by the Aerodyne Aerosol Chemical Speciation Monitor (ACSM) at NCNST. The POA and SOA concentrations are obtained from the ACSM measurements analyzed using the Positive Matrix Factorization (PMF) method. The SWDOWN and UVDOWN are measured by CM-11 pyranometers at five sites from Chinese Ecosystem Research Network (CERN) in the NCP, including Beijing, Luancheng, Yucheng, Jiaozhouwan, and Fengqiu (Fig. S1b) (41).

The hourly measurements of organic carbon (OC), elemental carbon (EC), sulfate, nitrate, and ammonium aerosols during the wintertime from 2013 to 2015 in Beijing have also been analyzed in this study. The hourly OC and EC concentrations are measured using a thermal/optical reflectance carbon analyzer (OCEC RT-4, Sunset Lab, USA) at Chinese Research Academy of Environmental Sciences (CRAES, 40.04°N, 116.40°E) in Beijing (42, 43). Hourly sulfate, nitrate, ammonium, and other inorganic ions are sampled and analyzed by ion chromatography (URG 9000S, Thermo Fisher Scientific, USA) at CRAES (44).

SI-2.2 Statistical metrics for observation-model comparisons

In the present study, the mean bias (*MB*), root mean square error (*RMSE*), the index of agreement (*IOA*), and correlation efficient (*R*) are used as indicators to evaluate the performance of WRF-Chem model in simulations against measurements. *IOA* describes the relative difference between the model and observation, ranging from 0 to 1, with 1 indicating perfect agreement.

$$\boldsymbol{MB} = \frac{\mathbf{1}}{\boldsymbol{N}}\sum_{\boldsymbol{i=1}}^{\boldsymbol{N}}(\boldsymbol{P_i} - \boldsymbol{O_i}) \quad (5)$$

$$\boldsymbol{RMSE} = \left[\frac{\mathbf{1}}{\boldsymbol{N}}\sum_{\boldsymbol{i=1}}^{\boldsymbol{N}}(\boldsymbol{P_i} - \boldsymbol{O_i})^{\mathbf{2}}\right]^{\frac{\mathbf{1}}{\mathbf{2}}} \quad (6)$$

$$IOA = 1 - \frac{\sum_{i=1}^{N}(P_i - O_i)^2}{\sum_{i=1}^{N}(|P_i - \bar{O}| + |O_i - \bar{O}|)^2} \quad (7)$$

$$R = \frac{\sum_{i=1}^{N}[(P_i - \bar{P}) \times (O_i - \bar{O})]}{\sqrt{\sum_{i=1}^{N}(P_i - \bar{P})^2 \times \sum_{i=1}^{N}(O_i - \bar{O})^2}} \quad (8)$$

Where P_i and O_i are the predicted and observed pollutant concentrations, respectively. *N* is the total number of the predictions used for comparisons, and $\bar{P}$ and $\bar{O}$ represents the average of the prediction and observation, respectively.

SI-3 Model performance

SI-3.1 Air pollutants simulations in the NCP

Fig. S2 shows the temporal profiles of observed and calculated near-surface $PM_{2.5}$, O_3, NO_2, SO_2 and CO concentrations averaged over monitoring sites in the NCP from 05 December 2015 to 04 January 2016. The model generally tracks well the diurnal variation of near-surface $PM_{2.5}$ concentrations ([$PM_{2.5}$]) in the NCP, with an *IOA* of 0.94, but slightly overestimates [$PM_{2.5}$], with a *MB* of 8.3 μg m^{-3}. The model successfully reproduces the temporal variations of near-surface O_3 concentrations compared to observations in the NCP, e.g., peak O_3 concentrations in the afternoon due to active photochemistry and low O_3 concentrations during nighttime caused by the NO_x titration, with an *IOA* of 0.94. However, the model generally underestimates the O_3 concentration during nighttime, with a *MB* of -3.6 μg m^{-3}. The model also reasonably well yields the NO_2 diurnal profiles with peaks in the evening, with an *IOA* of 0.86 and a *MB* of 1.6 μg m^{-3}, but sometimes there are considerable overestimations and underestimations. The model generally performs reasonably well in predicting the temporal variation of SO_2 concentrations against measurements, with an *IOA* of 0.74. However, considering that SO_2 is mainly emitted from point sources and its simulations are more sensitive to the wind field uncertainties (45), the overestimation and underestimation for the SO_2 simulation are rather large, with the *RMSE* of 13.3 μg m^{-3}.

Compared with measurements, the temporal profile of the near-surface CO concentration in the NCP is well simulated, with the *IOA* and *MB* of 0.87 and 0.1 μg m^{-3}, respectively.

SI-3.2 Spatial simulations of air pollutants in the NCP

Fig. S3 presents the spatial pattern of calculated and observed average near-surface concentrations of $PM_{2.5}$, O_3, NO_2, and SO_2 along with simulated winds from 05 December 2015 to 04 January 2016 in Eastern China. In general, the simulated air pollutants distributions are in good agreement with the measurements, but model biases still exist. The simulated winds are weak or calm during the simulation period, facilitating accumulation of air pollutants and causing the serious air pollution in Eastern China. The NCP is the most polluted region in Eastern China due to its massive air pollutants emissions, with the average near-surface [$PM_{2.5}$] generally exceeding 115 μg m^{-3}. The highest average near-surface [$PM_{2.5}$] of more than 150 μg m^{-3} are observed in Beijing, Hebei, Henan, Shandong, and the Guanzhong basin, which are well reproduced by the model. The simulated O_3 concentrations are rather low in the NCP, ranging from 5 to 40 μg m^{-3}, consistent with measurements. The low O_3 concentration during wintertime haze episodes in the NCP is primarily caused by the weak insolation further attenuated by clouds and aerosols, the titration of high NO_x emissions, and lack of the O_3 transport from outside (46). Although significant effort has been made to mitigate air pollutants emissions in the NCP, the observed and simulated average NO_2 and SO_2 concentrations are still high, varying from 30 to 100 μg m^{-3} and 20 to 100 μg m^{-3}, respectively. Interestingly, the simulated high SO_2 concentrations are mainly concentrated in cities and their surrounding areas, but the uniform distribution of NO_2 concentrations is predicted in the NCP, showing the substantial contribution of area sources.

SI-3.3 Aerosol species simulations in Beijing

Fig. S4 provides the temporal variations of simulated and observed aerosol species at NCNST in Beijing from 05 December 2015 to 04 January 2016. Generally, the WRF-Chem

model predicts reasonably the temporal variations of the aerosol species against the measurements. The WRF-Chem model yields the main peaks of the POA concentration compared to observations in Beijing, but frequently underestimates or overestimates the POA concentration, with an *IOA* of 0.80 and a *RMSE* of 17.4 μg m^{-3}. The POA level in Beijing is influenced by local emissions and to a large extent trans-boundary transport from outside during haze days, so its simulation is sensitive to uncertainties from emissions and meteorological fields (47, 48). The model still has difficulties in simulating the SOA concentrations, although the VBS modeling method is used and contributions from glyoxal and methylglyoxal are included in the study, with the *IOA* and *MB* of 0.77 and -10.6 μg m^{-3}, respectively. Except the SOA formation and transformation mechanism in the atmosphere, which remains elusive, many factors have potentials to influence the SOA simulation, such as meteorology, measurements, precursors emissions, and SOA treatments (4). The model tracks reasonably the temporal variation of the observed sulfate concentrations, and the *MB* and *IOA* are 0.6 μg m^{-3} and 0.90, respectively. Aside from SO_2 emissions and simulated meteorological fields, the SO_2 oxidation mechanism in the atmosphere also plays an important role in the sulfate simulation. In addition to direct emissions and SO_2 gas-phase oxidations by hydroxyl radicals (OH) and stabilized criegee intermediates (sCI), the SO_2 oxidation in aerosol water by O_2 catalyzed by Fe^{3+} is considered (49). Recent studies have proposed that the aqueous oxidation of SO_2 by NO_2 under the condition of high relative humidity (RH) and NH_3 neutralization could interpret the efficient sulfate formation during wintertime haze events (50, 51). However, the mechanism is still not included in this study, which might further improve the sulfate simulation. The model performs well in simulating the nitrate and ammonium concentrations against observations in Beijing, with *IOAs* of 0.90 and 0.91, respectively. Fig. S5 further provides the temporal variation of the simulated and observed BC concentrations at CRAES in Beijing from 05 December 2015 to 04 January

2016. Generally, the model simulates reasonably the temporal variation of BC concentrations compared to measurements in Beijing, but there also exists considerable underestimation or overestimation, with the *IOA* and *MB* of 0.78 and 0.2 μg m^{-3}. As a primary species, the BC concentration in Beijing depends on the contribution of local emissions and trans-boundary transport. Therefore, biases of the BC simulation might be caused mainly by uncertainties in emissions and the simulated wind fields.

SI-3.4 Aerosol radiative properties simulations in the NCP

Aerosol radiative forcing mainly depends on AOD, SSA, and asymmetry parameter. The model validations of AOD and SSA are provided in this study to further evaluate the aerosol radiative effect on the air pollution. The daily AOD at 550 nm, retrieved from Terra- and Aqua- MODIS level 2 products, is compared with the simulation. Fig. S6a shows the scatter plot of the daily retrieved and simulated AOD averaged in the NCP from 05 December 2015 to 04 January 2016. The simulated daily average AOD correlates well with the observation, with a correlation coefficient of 0.86. Generally, the retrieved and simulated AOD increases with deterioration of the haze pollution, but the model considerably underestimates the AOD against the observation. Fig. S6b presents the Taylor diagram (52) to show the variance, bias and correlation of the simulated and retrieved AOD from 05 December 2015 to 04 January 2016. There exists a good relationship between the simulated and retrieved daily AOD during the study episode, with correlation coefficients generally ranging from 0.5 to 0.9, and standard deviation mostly varying from 0.25 to 1.0. Fig. S7 shows the pattern comparison of the retrieved and simulated AOD averaged during the simulation period. The model reasonably reproduces the AOD distribution compared to the observations in the NCP, but considerably underestimates the AOD. The simulated and retrieved AOD averaged in the NCP during the simulation period is 0.43 and 0.59, respectively. It is worth noting that the simulated AOD is not only dependent on the column aerosol content and constituent, but also

267 significantly influenced by RH controlling the aerosol hydroscopic growth. Additionally, the
268 satellite retrieved AOD is subject to contamination by existence of clouds, and considering
269 the high occurrence frequency of clouds during haze days, the retrieved AOD is generally
270 higher than the simulation (53-55).

271 Aerosols are the mixture of absorbing and scattering constituents in the atmosphere.
272 Their radiative effect of cooling or warming the atmosphere relies on many parameters, and
273 SSA is one of the most important parameters (56). Fig. S8 depicts the comparison of the
274 measured and simulated diurnal profiles of SSA at 520nm at NCNST in Beijing during the
275 episodes. The model performs reasonably in simulating the daily variation of SSA in Beijing,
276 with an *IOA* of 0.69 and a *MB* of 0.0, but the overestimation or underestimation is rather
277 large. SSA is the ratio of aerosol scattering to extinction, which is highly sensitive to the
278 relative distribution of scattering and absorbing aerosol constituents in the atmosphere, and
279 the RH determining the hygroscopic growth of aerosols. Therefore, the uncertainties of the
280 simulated SSA probably originate from the model biases of aerosol constituents and the RH.

281 **SI-3.5 Cloud properties**

282 Clouds are one of the most important factors affecting the solar radiation reaching the
283 ground. Fig. S9 presents the scatter plot of the daily retrieved and simulated CF and COT
284 averaged in the NCP from 05 December 2015 to 31 December 2015. Generally, the simulated
285 daily average CF correlates well with that retrieved, with a correlation coefficient of 0.64
286 (Fig. S9a). The correlation between the simulated and retrieved COT is not as good as that of
287 the CF, with a coefficient of 0.52 (Fig. S9b). The model generally underestimates the CF and
288 COT compared with those retrieved from the MODIS measurements, causing the model
289 overestimation of SWDOWN and UVDOWN. The simulated average CF and COT over the
290 NCP during the episode are 47.8% and 11.9, lower than the MODIS retrieved 78.4% and
291 15.0, respectively. Numerical models still have difficulties in representing accurately clouds

292 in terms of microphysical processes, cloud morphologies, occurrence and dissipation. In
293 addition, many uncertainties also significantly impact CF and COT retrievals, such as the
294 satellite's view zenith angle, cloud microphysics assumptions, namely cloud phase, particle
295 size and shape, et al. (57-60). Therefore, it is still difficult to validate cloud simulations using
296 the satellite cloud products.

297 **SI-3.6 Downward solar radiation simulations in North China Plain**

298 Fig. S10 presents the daily profiles of simulated and observed SWDOWN at the ground
299 surface in Beijing, Jiaozhouwan, Luancheng, and Yuancheng from 05 December 2015 to 04
300 January 2016. The WRF-Chem model simulates well the daily variation of SWDOWN,
301 especially in Jiaozhouwan, Luancheng, and Yucheng, with *IOAs* around 0.90. The model is
302 subject to overestimating the SWDOWN against measurements, with *MB*s ranging from 6.3
303 to 86.2 W m^{-2}. The SWDOWN reaching the ground surface is very sensitive to the cloud
304 cover and optical thickness. However, the WRF-Chem model still has difficulties in
305 accurately predicting the CF and COT, which might constitute one of the most important
306 reasons for model biases of the SWDOWN (please reference SI-3.5). In addition, the
307 horizontal resolution used in simulations cannot adequately resolve the cumulus clouds, also
308 causing uncertainties in the simulations of the SWDOWN.

309 **SI-3.7 PBLH simulations in Beijing**

310 Fig. S11 shows the temporal variations of the observed and simulated PBLH at a
311 meteorological site in Beijing from 05 December 2015 to 04 January 2016. The average
312 PBLH at 12:00 Beijing Time (BJT) during the episode at the meteorological site is 465.2 m,
313 with the minimum of 101.8 m and the maximum of 1017.9 m, showing decreased PBLH
314 during the haze episode. In general, the WRF-Chem model tracks reasonably the daily
315 variation of the PBLH in Beijing, with an *IOA* of 0.70. However, the model has difficulties in
316 reproducing the observed very low PBLH, e.g., less than 200 m. The PBLH varies

substantially with time due to many factors including large-scale dynamics, cloudiness, convective mixing, and the diurnal cycle of solar radiation (61). Therefore, the simulation uncertainties of meteorological conditions constitute the main reason for the simulation bias of PBLH. For example, the overestimation of SWDOWN at 12:00 BJT (Figure 10a) probably causes the overestimation of PBLH in Beijing.

In general, the simulated variations of SWDOWN, PBLH, aerosol radiative properties, cloud properties, air pollutants ($PM_{2.5}$, O_3, NO_2, SO_2, CO) and aerosol species are in good agreement with observations, indicating that the simulations of meteorological conditions, chemical processes and the emission inventory used in the WRF-Chem model are reasonable, providing a reliable basis for the further investigation.

SI-4 Relationship of UVDOWN and O_3 with $PM_{2.5}$

Fig. S15a shows the scatter plot of the observed UVDOWN and near-surface [$PM_{2.5}$] in Beijing, Fengqiu, Jiaozhouwan, Luancheng, and Yucheng at noon (11:00-13:00 LT) under sunny weather conditions from 05 December 2015 to 04 January 2016. Excluding the effect of clouds on the UVDOWN, the decrease of the UVDOWN with near-surface [$PM_{2.5}$] is evident, especially when near-surface [$PM_{2.5}$] are less than 300 μg m^{-3}. With near-surface [$PM_{2.5}$] increasing from several to 300 μg m^{-3}, the UVDOWN rapidly decreases from 20 to 5 W m^{-2}, indicating that increasing aerosols in the atmosphere efficiently decrease the UVDOWN. The fitted trend line between the UVDOWN and near-surface [$PM_{2.5}$] also shows a significant decrease of the UVDOWN with increasing [$PM_{2.5}$]. It is worth noting that near-surface [$PM_{2.5}$] might not well represent the aerosol content in the whole vertical atmospheric layer and the aerosol optical properties also vary day by day, so there exists a large dispersion of the UVDOWN against the fitted line. Decreasing UVDOWN caused by the atmospheric aerosols reduces photolysis rates and hinders the near-surface O_3 formation,

as shown in Fig. S15b. The large dispersion of observed near-surface O_3 concentrations against the fitted trend line might be caused by variations of background O_3, volatile organic compounds and NO_x levels at the four observation sites.

SI-5 Model uncertainties

In the Base scenario, ARI contribute additional 7.8% of near-surface $PM_{2.5}$, but API suppress secondary aerosol formation and decrease near-surface $PM_{2.5}$ by 4.2%. The combination of ARI and API causes only a 4.8% net increase of $PM_{2.5}$ or API reduce 38.5% of $PM_{2.5}$ enhancement due to ARI. Although the good performance of the WRF-Chem model in simulating the heavy haze episode provides a reliable basis for evaluation of the ARI, API, and their synergy effect on PM pollution, many uncertainties in model simulations have large potentials to impact the evaluation result, i.e. the API weakening effect on $PM_{2.5}$ enhancement due to ARI, including those in meteorological conditions, emissions, potential missing chemical mechanisms, particle interactions with solar radiation (such as the BC morphology, the brown carbon (BrC) absorption, aerosol mixing state assumption), and aerosol-cloud interaction. Therefore, we have conducted additional 11 sensitivity scenarios to quantify model uncertainties to warrant convincing evaluation results.

SI-5.1 Impacts of meteorological conditions

Meteorological conditions play a key role in the formation of PM pollution, determining dispersion or accumulation of air pollutants (45). In order to quantify impacts of meteorological conditions on the contribution of API and ARI to near-surface [$PM_{2.5}$], two sensitivity scenarios, Met-2016 and Met-2017, have been conducted with meteorological conditions in December of 2016 and 2017, respectively, based on the 2015 emission inventory. The model configuration in Met-2016 and Met-2017 is the same as that of the Base scenario. In the Met-2016 scenario, the average contribution of API, ARI, and both ARI

and API to near-surface [$PM_{2.5}$] is -3.6%, 7.4%, and 5.2% during the simulation period in the NCP, respectively, with an API weakening effect of 29.8%, which is lower than that of the Base scenario (Table S3). In the Met-2017 scenario, the average contribution of API, ARI, and both ARI and API to near-surface [$PM_{2.5}$] is -2.8%, 4.6%, and 2.7%, respectively, with an API weakening effect of 41.3%, which is higher than that in the Base scenario.

SI-5.2 Impacts of anthropogenic emissions

The Chinese government has made great efforts to reduce emissions of air pollutants by implementing strict mitigation measures since 2013, and except non-methane volatile organic compounds (NMVOCs) and NH_3, the anthropogenic emissions of SO_2, NO_x, CO, and $PM_{2.5}$ have decreased considerably from 2013 to 2017 (62, 63). Two sensitivity scenarios, Emiss-Inc and Emiss-Dec, have been performed with the anthropogenic emissions increased and decreased by 25%, respectively, to evaluate impacts of emissions on the contribution of API and ARI to near-surface [$PM_{2.5}$]. In the Emiss-Dec scenario, when the anthropogenic emissions are decreased by 25%, the average near-surface $PM_{2.5}$ contribution caused by API, ARI, and both ARI and API are -3.1%, 7.7%, and 4.8%, respectively, with an API weakening effect of 37.6% (Table S3). With the anthropogenic emissions increased by 25% in the Emiss-Inc scenario, the average near-surface $PM_{2.5}$ contribution caused by API, ARI, and both ARI and API are -4.6%, 9.3%, and 4.6%, respectively, with an API weakening effect of 50.5%.

SI-5.3 Impacts of potential missing chemical assumption

The WRF-Chem model simulates well the temporal variations of sulfate, nitrate, and ammonium concentrations, but it substantially underestimates the SOA concentration against the measurement in Beijing, with a *MB* of -10.6 μg m^{-3} (Fig. S4). Therefore, a sensitivity scenario, SOA-Fast, is devised to consider impacts of the potential missing chemical mechanism of the SOA formation on the API weakening effect. Huang et al. (64) have shown

that low temperature does not substantially decrease SOA formation rates of biomass burning emissions chemistry with the formation rate constant via OH radical of (2.5-6.7) $\times 10^{-11}$ cm^3 $molecule^{-1}$ s^{-1}. In the Base scenario, the aging rate constant via OH radical of primary organic gases (POGs) and intermediate volatile organic compounds (IVOCs) from traffic-related combustion and biomass burning emissions is set to be 2.0×10^{-11} cm^3 $molecule^{-1}$ s^{-1} (4). Therefore, in the SOA-Fast scenario, the rate constant of POGs and IVOCs with OH radical is set to be 6.7 $\times 10^{-11}$ cm^3 $molecule^{-1}$ s^{-1} to quantify the impact of uncertainties from the potential missing chemical mechanism on the API weakening effect. The simulated SOA in the base case of the SOA-Fast scenario is increased by 50% compared to those in the base case of the Base scenario on average in the NCP during the episode. In the SOA-Fast scenario, the average contribution of API, ARI, and both ARI and API to near-surface [$PM_{2.5}$] is -4.9%, 8.4%, and 4.5%, respectively, with an API weakening effect of 46.4%, showing that the API weakening effect is enhanced when the SOA simulation is improved (Table S3).

SI-5.4 Impacts of BC morphology

BC aerosols exert a great impact on air quality and climate change because of its high absorption. The radiative properties of BC aerosols depend largely on its morphology during the aging process. The aging process of BC aerosols results in a dramatic change in morphology (65). BC aging includes the initial transformation from a fractal to sphere morphology with little variation of absorption and subsequent growth of fully compact particles with an obvious enhancement of absorption (66). In the Base scenario, the aging process and the variation of particle morphology are both considered in the WRF-Chem model (SI-1.3). We have further performed a sensitivity scenario (referred to as BC-No-Morph) to assess impacts of variation of BC morphology on the API weakening effect, in which BC aerosols are assumed not to undergo morphology variation, with a constant effective density of 1.8 g cm^{-3}. In the BC-No-Morph scenario, the average

417 contribution of API, ARI, and both ARI and API to near-surface [$PM_{2.5}$] is -3.4%, 8.1%, and
418 5.5%, respectively, with an API weakening effect of 32.1%, indicating that the BC
419 morphology variation appreciably affects the API weakening effect (Table S3).

420 **SI-5.5 Impacts of aerosol mixing states**

421 The radiative properties of aerosols depend largely on the mixing state, and the mixing
422 state of aerosols in the atmosphere varies between the completely internal and external
423 mixing. In the Base scenario, we categorize aerosols into four types: (1) internally mixed
424 sulfate, nitrate, ammonium, hydrophilic organics and black carbon, and water; (2)
425 hydrophobic organics; (3) hydrophobic black carbon; and (4) other unidentified aerosols
426 (dust-like). These four kinds of aerosols are assumed to be mixed externally. In order to
427 quantify impacts of aerosol mixing states on the API weakening effect, two sensitivity
428 scenarios, Aero-Ext-Mix and Aero-Int-Mix, have been performed, with the assumption that
429 aerosols are completely externally and internally mixed, respectively. In the Aero-Int-Mix
430 scenario, the average contribution of API, ARI, and both ARI and API to near-surface [$PM_{2.5}$]
431 is -4.7%, 7.1%, and 3.4%, respectively, with an API weakening effect of 52.1%, showing that
432 the API weakening effect is enhanced when the aerosol absorption is increased caused by
433 completely internal mixing aerosols (Table S3). However, when the aerosols are assumed to
434 be completely externally mixed in the Aero-Ext-Mix scenario, the API weakening effect is
435 substantially decreased, about 13.6% due to decreased aerosol absorption.

436 **SI-5.6 Impacts of BrC absorption**

437 As a kind of OA, BrC mainly have a higher absorption at shorter wavelengths, which is
438 different from BC aerosols with a relatively flat absorption spectrum (67). There are still
439 large uncertainties in the absorption properties of BrC aerosols (68, 69). Therefore, two
440 sensitivity scenarios, BrC-Abs-High and BrC-Abs-Low, are performed to consider impacts of
441 BrC absorption on the API weakening effect, in which the imaginary indices of OA are

increased and decreased by 50%, respectively. In the BrC-Abs-High scenario with the higher BrC absorption，the average contribution of API, ARI, and both ARI and API to near-surface [$PM_{2.5}$] is -4.5%, 7.3%, and 4.3%, respectively, with an API weakening effect of 41.1%, while in the BrC-Abs-Low scenario with the lower BrC absorption, the contribution of API, ARI, and both ARI and API is -4.5%, 7.7%, and 4.8%, respectively, with an API weakening effect of 37.7% (Table S3).

SI-5.7 Impacts of aerosol-cloud interaction

In the Base scenario, the one-moment bulk microphysics scheme of Hong et al. (15) is used, without consideration of aerosol effects on cloud development. However, aerosol-cloud interaction (ACI) have large potentials to alter the API weakening effect, through perturbing the dynamic fields, aerosol activation to CCN and IN, and changing the precipitation distribution and further washout of aerosols. In order to evaluate impacts of ACI on the API weakening effect, we have further performed a sensitivity scenario (referred to as ACI-2M), in which a two-moment bulk microphysics scheme with aerosol effects on clouds (31, 40) is used. When considering ACI in the ACI-2M scenario, the average contribution of API, ARI, and both ARI and API to near-surface [$PM_{2.5}$] is -3.3%, 6.5%, and 3.9%, respectively, with an API weakening effect of 40.0%, which is close to that of the Base scenario.

SI-5.8 API effect on surface temperature and the temperature-dependent chemistry

Temperature is a key meteorological parameter affecting the atmospheric physical and chemical process. The API effect decreases the aerosol concentration through reducing photolysis rates to suppress secondary aerosol formation, further affecting the air temperature and the temperature-dependent chemistry. Fig. S20 presents the vertical profile of the average temperature perturbation caused by the API effect in the NCP from 05 December 2015 to 04 January 2016. On average, the API effect increases the temperature by 0.01℃ to 0.03℃ in the PBL and decreases the temperature by around 0.005℃ to 0.02℃ above the PBL. In order

to evaluate impacts of the temperature perturbation caused by the API effect, a sensitivity experiment based on the base case of the Base scenario has been conducted, in which the calculation of chemical reaction rate constant depending on temperature includes the temperature perturbation caused by the API effect. The temperature perturbation due to the API effect decreases near-surface [$PM_{2.5}$] by 0.3 μg m^{-3} or 0.2% on average in the NCP during the study episode, showing that the temperature perturbation induced by the API effect does not substantially influence the temperature-dependent chemistry.

SI-5.9 Cloud variations due to the ARI and API effect

The ARI and API effect not only alter the aerosol concentration and distribution in the PBL, also perturb the temperature and wind field, which could influence clouds and radiation, further modifying photolysis. Fig. S21 presents the daily variation of the average daytime COT and CF caused by the API and API effect in the NCP from 05 December 2015 to 04 January 2016. The API effect generally increases the COT and CF during the episode slightly, with an average enhancement of 0.09 and 0.12%, respectively. Therefore, the API effect is decreased slightly by enhancement of the COT and CF caused by itself, The ARI effect increases the average COT by 0.073 and decreases the average CF by 0.73%.

References

1. Grell GA, et al. (2005) Fully coupled "online" chemistry within the WRF model. *Atmos Environ* 39:6957-6975.
2. Li G, et al. (2010) Impacts of HONO sources on the photochemistry in Mexico City during the MCMA-2006/MILAGO Campaign. *Atmos Chem Phys* 10:6551-6567.
3. Li G, Bei N, Tie X, Molina LT (2011) Aerosol effects on the photochemistry in Mexico City during MCMA-2006/MILAGRO campaign. *Atmos Chem Phys* 11:5169-5182.
4. Li G, et al. (2011) Simulations of organic aerosol concentrations in Mexico City using the WRF-CHEM model during the MCMA-2006/MILAGRO campaign. *Atmos Chem Phys* 11:3789-3809.
5. Binkowski FS, Roselle SJ (2003) Models-3 community multiscale air quality (CMAQ) model aerosol component - 1. Model description. *J Geophys Res Atmos* 108:4183.
6. Kulmala M, Laaksonen A, Pirjola L (1998) Parameterizations for sulfuric acid/water nucleation rates. *J Geophys Res Atmos* 103:8301-8308.
7. Wesely ML (1989) Parameterization of surface resistances to gaseous dry deposition in regional-scale numerical models. *Atmos Environ* 23:1293-1304.
8. Li GH, Zhang RY, Fan JW, Tie XX (2005) Impacts of black carbon aerosol on photolysis and ozone. *J Geophys Res Atmos* 110: D23206.
9. Nenes A, Pandis SN, Pilinis C (1998) ISORROPIA: A new thermodynamic equilibrium model for multiphase multicomponent inorganic aerosols. *Aquat Geochem* 4:123-152.
10. Shrivastava MK, Lane TE, Donahue NM, Pandis SN, Robinson AL (2008) Effects of gas particle partitioning and aging of primary emissions on urban and regional organic aerosol concentrations. *J Geophys Res Atmos* 113: D18301.
11. Robinson AL, et al. (2007) Rethinking organic aerosols: Semivolatile emissions and photochemical aging. *Science* 315:1259-1262.
12. Liggio J, Li SM, McLaren R (2005) Reactive uptake of glyoxal by particulate matter. *J Geophy Res Atmos* 110: D10304.
13. Zhao J, Levitt NP, Zhang RY, Chen JM (2006) Heterogeneous reactions of methylglyoxal in acidic media: Implications for secondary organic aerosol formation. *Environ Sci Technol* 40:7682-7687.
14. Volkamer R, et al. (2007) A missing sink for gas-phase glyoxal in Mexico City: Formation of secondary organic aerosol. *Geophys Res Lett* 34: L19807.
15. Hong SY, Lim JOJ (2006) The WRF Single-Moment 6-Class Microphysics Scheme (WSM6). *Asia Pac J Atmos Sci* 42:129-151.
16. Janjić ZI (2002) Nonsingular Implementation of the Mellor–Yamada Level 2.5 Scheme in the NCEP Meso Model. *Ncep Office Note* 436.
17. Chen F, Dudhia J (2001) Coupling an advanced land surface-hydrology model with the Penn State-NCAR MM5 modeling system. Part I: Model implementation and sensitivity. *Mon Weather Rev* 129:569-585.
18. Chou MD and Suarez MJ (2001) A Thermal Infrared Radiation Parameterization for Atmospheric Studies. *NASA/TM-2001-104606* Vol.19, 55pp.

19. Chou MD, Suarez MJ (1999) A solar radiation parameterization for atmospheric studies. *NASA/TM-1999-10460, Nasa Tech Rep* Vol.15, 38pp.
20. Horowitz LW, et al. (2003) A global simulation of tropospheric ozone and related tracers: Description and evaluation of MOZART, version 2. *J Geophys Res Atmos* 108:4784.
21. Zhang Q, et al. (2009) Asian emissions in 2006 for the NASA INTEX-B mission. *Atmos Chem Phys* 9:5131-5153.
22. Li GH, et al. (2017) Widespread and persistent ozone pollution in eastern China during the non-winter season of 2015: observations and source attributions. *Atmos Chem Phys* 17:2759-2774.
23. Guenther A, et al. (2006) Estimates of global terrestrial isoprene emissions using MEGAN (Model of Emissions of Gases and Aerosols from Nature). *Atmos Chem Phys* 6:3181-3210.
24. Wiedinmyer C, et al. (2006) Estimating emissions from fires in North America for air quality modeling. *Atmos Environ* 40:3419-3432.
25. Wiedinmyer C, et al. (2011) The Fire INventory from NCAR (FINN): a high resolution global model to estimate the emissions from open burning. *Geosci Model Dev* 4:625-641.
26. D'Almeida GA, Koepke P, Shettle EP (1991) Atmospheric aerosols: Global climatology and radiative characteristics. *J Med Microbiol* 54:55-61.
27. Moffet RC, Prather KA (2009) In-situ measurements of the mixing state and optical properties of soot with implications for radiative forcing estimates. *Proc Natl Acad Sci USA* 106:11872-11877.
28. Cooke WF, Wilson JJN (1996) A global black carbon aerosol model. *J Geophys Res Atmos* 101:19395-19409.
29. Barnard JC, Volkamer R, Kassianov EI (2008) Estimation of the mass absorption cross section of the organic carbon component of aerosols in the Mexico City Metropolitan Area. *Atmos Chem Phys* 8:6665-6679.
30. Kirchstetter TW, Novakov T, Hobbs PV (2004) Evidence that the spectral dependence of light absorption by aerosols is affected by organic carbon. *J Geophys Res Atmos* 109: D21208.
31. Li GH, Wang Y, Zhang RY (2008) Implementation of a two-moment bulk microphysics scheme to the WRF model to investigate aerosol-cloud interaction. *J Geophys Res Atmos* 113: D15211.
32. Petters MD, Kreidenweis SM (2007) A single parameter representation of hygroscopic growth and cloud condensation nucleus activity. *Atmos Chem Phys* 7:1961-1971.
33. Petters MD, Kreidenweis SM (2008) A single parameter representation of hygroscopic growth and cloud condensation nucleus activity - Part 2: Including solubility. *Atmos Chem Phys* 8:6273-6279.
34. Petters MD, Kreidenweis SM (2013) A single parameter representation of hygroscopic growth and cloud condensation nucleus activity - Part 3: Including surfactant partitioning. *Atmos Chem Phys* 13:1081-1091.
35. Rogers RR, Yau MK (1989) *A short course in cloud physics* (Pergamon, Tarrytown,

New York).
36. Pruppacher HR, Klett JD (1997) *Microphysics of Clouds and Precipitation, Second Revised and Enlarged Edition with an Introduction to Cloud Chemistry and Cloud Electricity* (Kluwer Academic Publishers, Reidel, Dordrecht, 954 pp).
37. Khain AP (2000) Notes on state-of-the-art investigations of aerosol effects on precipitation: a critical review. *Environ Res Lett* 4:015004.
38. Phillips VTJ, DeMott PJ, Andronache C (2008) An empirical parameterization of heterogeneous ice nucleation for multiple chemical species of aerosol. *J Atmos Sci* 65:2757-2783.
39. Phillips VTJ, et al. (2013) Improvements to an Empirical Parameterization of Heterogeneous Ice Nucleation and Its Comparison with Observations. *J Atmos Sci* 70:378-409.
40. Zhou X, et al. (2017) Aerosol Effects on the Development of Cumulus Clouds over the Tibetan Plateau. *Atmos Chem Phys* 17:7423-7434.
41. Liu H, Hu B, Zhang L, Wang YS, Tian PF (2016) Spatiotemporal characteristics of ultraviolet radiation in recent 54years from measurements and reconstructions over the Tibetan Plateau. *J Geophys Res Atmos* 121:7673-7690.
42. Wei S, et al. (2014) Field measurement on the emissions of PM, OC, EC and PAHs from indoor crop straw burning in rural China. *Environ Pollut* 184:18-24.
43. Liu W, et al. (2018) Air pollution and inhalation exposure to particulate matter of different sizes in rural households using improved stoves in central China. *J Environ Sci* 63:87-95.
44. Feng T, et al. (2019) Secondary organic aerosol enhanced by increasing atmospheric oxidizing capacity in Beijing-Tianjin-Hebei (BTH), China. *Atmos Chem Phys* 19:7429-7443.
45. Bei NF, et al. (2017) Impacts of meteorological uncertainties on the haze formation in Beijing-Tianjin-Hebei (BTH) during wintertime: a case study. *Atmos Chem Phys* 17:14579-14591.
46. Li X, et al. (2018) Contributions of residential coal combustion to the air quality in Beijing-Tianjin-Hebei (BTH), China: a case study. *Atmos Chem Phys* 18:10675-10691.
47. Bei N, Lei W, Zavala M, Molina LT (2010) Ozone predictabilities due to meteorological uncertainties in the Mexico City basin using ensemble forecasts. *Atmos Chem Phys* 10:6295-6309.
48. Bei N, Li G, Molina LT (2012) Uncertainties in SOA simulations due to meteorological uncertainties in Mexico City during MILAGRO-2006 field campaign. *Atmos Chem Phys* 12:11295-11308.
49. Li GH, et al. (2017) A possible pathway for rapid growth of sulfate during haze days in China. *Atmos Chem Phys* 17:3301-3316.
50. Wang G, et al. (2016) Persistent sulfate formation from London Fog to Chinese haze. *Proc Natl Acad Sci USA* 48:13630-13635.
51. Cheng YF, et al. (2016) Reactive nitrogen chemistry in aerosol water as a source of sulfate during haze events in China. *Sci Adv* 2: e1601530.
52. Taylor KE (2001) Summarizing multiple aspects of model performance in a single

diagram. *J Geophys Res Atmos* 106:7183-7192.
53. Engstrom A, Ekman AML (2010) Impact of meteorological factors on the correlation between aerosol optical depth and cloud fraction. *Geophys Res Lett* 37: L18814.
54. Chand D, et al. (2012) Aerosol optical depth increase in partly cloudy conditions. *J Geophys Res Atmos* 117: D17207.
55. Grandey BS, Stier P, Wagner TM (2013) Investigating relationships between aerosol optical depth and cloud fraction using satellite, aerosol reanalysis and general circulation model data. *Atmos Chem Phys* 13:3177-3184.
56. Satheesh SK, Vinoj V, Krishnamoorthy K (2010) Assessment of Aerosol Radiative Impact over Oceanic Regions Adjacent to Indian Subcontinent Using Multisatellite Analysis. *Adv Meteorol* 2010: 1-13.
57. An N, Wang KC (2015) A Comparison of MODIS-Derived Cloud Fraction with Surface Observations at Five SURFRAD Sites. *J Appl Meteorol Climatol* 54:1009-1020.
58. Platnick S, et al. (2017) The MODIS Cloud Optical and Microphysical Products: Collection 6 Updates and Examples From Terra and Aqua. *IEEE Trans Geosci Remote Sens* 55:502-525.
59. Zeng S, Cornet C, Parol F, Riedi J, Thieuleux F (2012) A better understanding of cloud optical thickness derived from the passive sensors MODIS/AQUA and POLDER/PARASOL in the A-Train constellation. *Atmos Chem Phys* 12:11245-11259.
60. Li Z, Cribb MC, Chang FL (2014) *Validation of MODIS-Retrieved Cloud Fractions Using Whole Sky Imager Measurements at the Three ARM Sites.* (Fourteenth ARM Science Team Meeting Proceedings, Albuquerque).
61. Sivaraman C, McFarlane S, Chapman E (2013) *Planetary boundary layer (PBL) height value added product (VAP): Radiosonde retrievals.* (U.S. DOE, Office of Science, Office of Biological and Environment Research, DOE/SC-ARM/TR-132).
62. Zheng B, et al. (2018) Trends in China's anthropogenic emissions since 2010 as the consequence of clean air actions. *Atmos Chem Phys* 18:14095-14111.
63. Zhang Q, et al. (2019) Drivers of improved $PM_{2.5}$ air quality in China from 2013 to 2017. *Proc Natl Acad Sci USA* 116:24463-24469.
64. Huang RJ, et al. (2014) High secondary aerosol contribution to particulate pollution during haze events in China. *Nature* 514:218-222.
65. Cheng TH, Wu Y, Chen H (2014) Effects of morphology on the radiative properties of internally mixed light absorbing carbon aerosols with different aging status. *Opt Express* 22:15904-15917.
66. Peng JF, et al. (2016) Markedly enhanced absorption and direct radiative forcing of black carbon under polluted urban environments. *Proc Natl Acad Sci USA* 113:4266-4271.
67. Li ZJ, et al. (2019) Light absorption properties and potential sources of particulate brown carbon in the Pearl River Delta region of China. *Atmos Chem Phys* 19:11669-11685.
68. Lack DA, Langridge JM (2013) On the attribution of black and brown carbon light absorption using the Angstrom exponent. *Atmos Chem Phys* 13:10535-10543.

69. Wang X, et al. (2016) Deriving brown carbon from multiwavelength absorption measurements: method and application to AERONET and Aethalometer observations. *Atmos Chem Phys* 16:12733-12752.

Table S1. WRF-Chem model configurations

Regions	East Asia
Study period	December 05, 2015 - January 04, 2016
Domain size	400 × 400
Domain center	35°N, 114°E
Horizontal resolution	12km × 12km
Vertical resolution	35 vertical levels with a stretched vertical grid with spacing ranging from 30 m near the surface, to 500 m at 2.5 km and 1 km above 14 km
Microphysics scheme	WSM 6-class graupel scheme (15)
Boundary layer scheme	MYJ TKE scheme (16)
Surface layer scheme	MYJ surface scheme (16)
Land-surface scheme	Unified Noah land-surface model (17)
Longwave radiation scheme	Goddard longwave scheme (18)
Shortwave radiation scheme	Goddard shortwave scheme (19)
Meteorological boundary and initial conditions	NCEP 1°×1° reanalysis data
Chemical initial and boundary conditions	MOZART 6-hour output (20)
Anthropogenic emission inventory	Developed by Zhang et al.(21) and Li et al. (22), 2012 base year, and SAPRC-99 chemical mechanism
Biogenic emission inventory	MEGAN model developed by Guenther et al. (23)
Biomass burning emission inventory	Fire Inventory from NCAR (FINN) (24, 25)
Model spin-up time	4 days and 4 hours (Simulations starting time: 12:00 UTC on November 30, 2015)

Table S2. Aerosol optical constants used in the calculation of aerosol optical properties.

Aerosols	Refractive Index (λ=380nm)	Refractive Index (λ=550nm)
Black carbon	1.75-0.75i	1.75-0.72i
Primary organic aerosol	1.55-0.14i	1.55-0.03i
Secondary organic aerosol	$1.55\text{-}2.0\times10^{-3}$i	$1.55\text{-}2.0\times10^{-3}$i
Sulfate	$1.44\text{-}1.0\times10^{-8}$i	$1.43\text{-}1.0\times10^{-8}$i
Nitrate	$1.44\text{-}1.0\times10^{-8}$i	$1.43\text{-}1.0\times10^{-8}$i
Ammonium	$1.44\text{-}1.0\times10^{-8}$i	$1.43\text{-}1.0\times10^{-8}$i
Water	$1.35\text{-}2.0\times10^{-9}$i	$1.34\text{-}2.5\times10^{-9}$i
Dust	$1.53\text{-}1.4\times10^{-2}$i	$1.53\text{-}5.5\times10^{-3}$i

685 **Table S3.** Model uncertainties on the API weakening effect
686

Scenario	API (%)	ARI (%)	API+ARI (%)	API Weakening effect (%)
Base[1]	-4.2	7.8	4.8	38.5
Met-2016[2]	-3.6	7.4	5.2	29.8
Met-2017[3]	-2.8	4.6	2.7	41.3
Emiss-Dec[4]	-3.1	7.7	4.8	37.6
Emiss-Inc[5]	-4.6	9.3	4.6	50.5
SOA-Fast[6]	-4.9	8.4	4.5	46.4
BC-No-Morph[7]	-3.4	8.1	5.5	32.1
Aero-Int-Mix[8]	-4.7	7.1	3.4	52.1
Aero-Ext-Mix[9]	-1.7	11.0	9.5	13.6
BrC-Abs-High[10]	-4.5	7.3	4.3	41.1
BrC-Abs-Low[11]	-4.4	7.7	4.8	37.7
ACI-2M[12]	-3.3	6.5	3.9	40.0

687 [1]Base scenario includes the base simulation with both ARI and API and additional three sensitivity
688 simulations without API, ARI, and both ARI and API. All the sensitivity scenarios are based on the Base
689 scenario.

690 [2]Meteorological conditions in December of 2016 is used.

691 [3]Meteorological conditions in December of 2017 is used.

692 [4]Anthropogenic emissions are decreased by 25%.

693 [5]Anthropogenic emissions are increased by 25%.

694 [6]The reaction rate constant of POGs and IVOCs with OH radical is set to be 6.7×10^{-11} cm^3 $molecule^{-1}$ s^{-1}.

695 [7]BC is assumed not to undergo morphology variation, with a constant effective density of 1.8 g cm^{-3}.

696 [8]Aerosols are assumed to be completely internally mixed.

697 [9]Aerosols are assumed to be completely externally mixed.

698 [10]The imaginary indices of OA are increased by 50%.

699 [11]The imaginary indices of OA are decreased by 50%.

700 [12]A two-moment bulk microphysics scheme with aerosol effects on clouds is used.
701
702
703
704
705

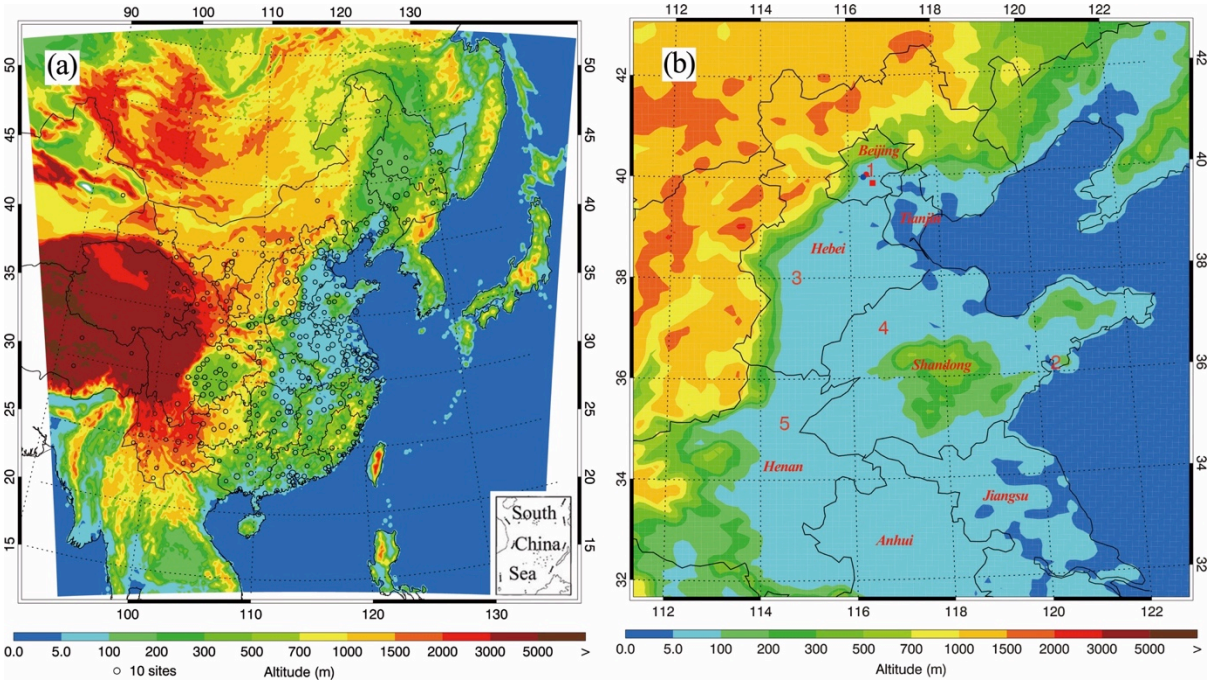

Fig. S1. (a) WRF-Chem simulation domain with topography and (b) North China Plain. In (a), the blue circles represent centers of cities with ambient monitoring sites and the size of blue circles denotes the number of ambient monitoring sites of cities. In (b), the red numbers denote the CERN sites with the solar radiation measurement. 1: Beijing; 2: Jiaozhouwan; 3: Luancheng; 4: Yucheng; 5: Fengqiu. The blue and red filled circles indicate the NCNST and CRAES site in Beijing, respectively, and the red filled rectangle denotes the meteorological site.

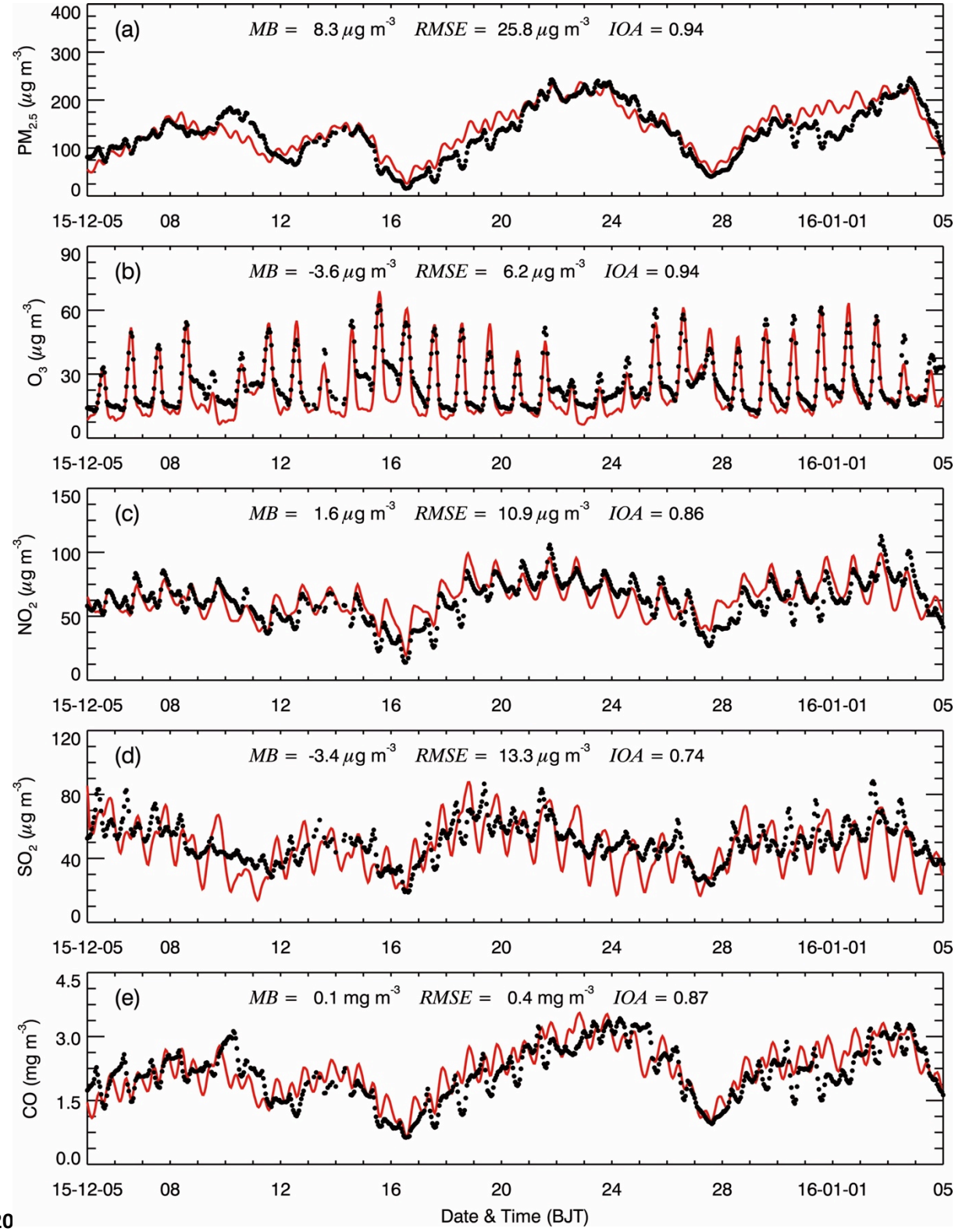

Fig. S2. Comparison of observed (black dots) and simulated (solid red lines) diurnal profiles of near-surface hourly mass concentrations of (a) $PM_{2.5}$, (b) O_3, (c) NO_2, (d) SO_2, and (d) CO averaged at monitoring sites in the NCP from 05 December 2015 to 04 January 2016.

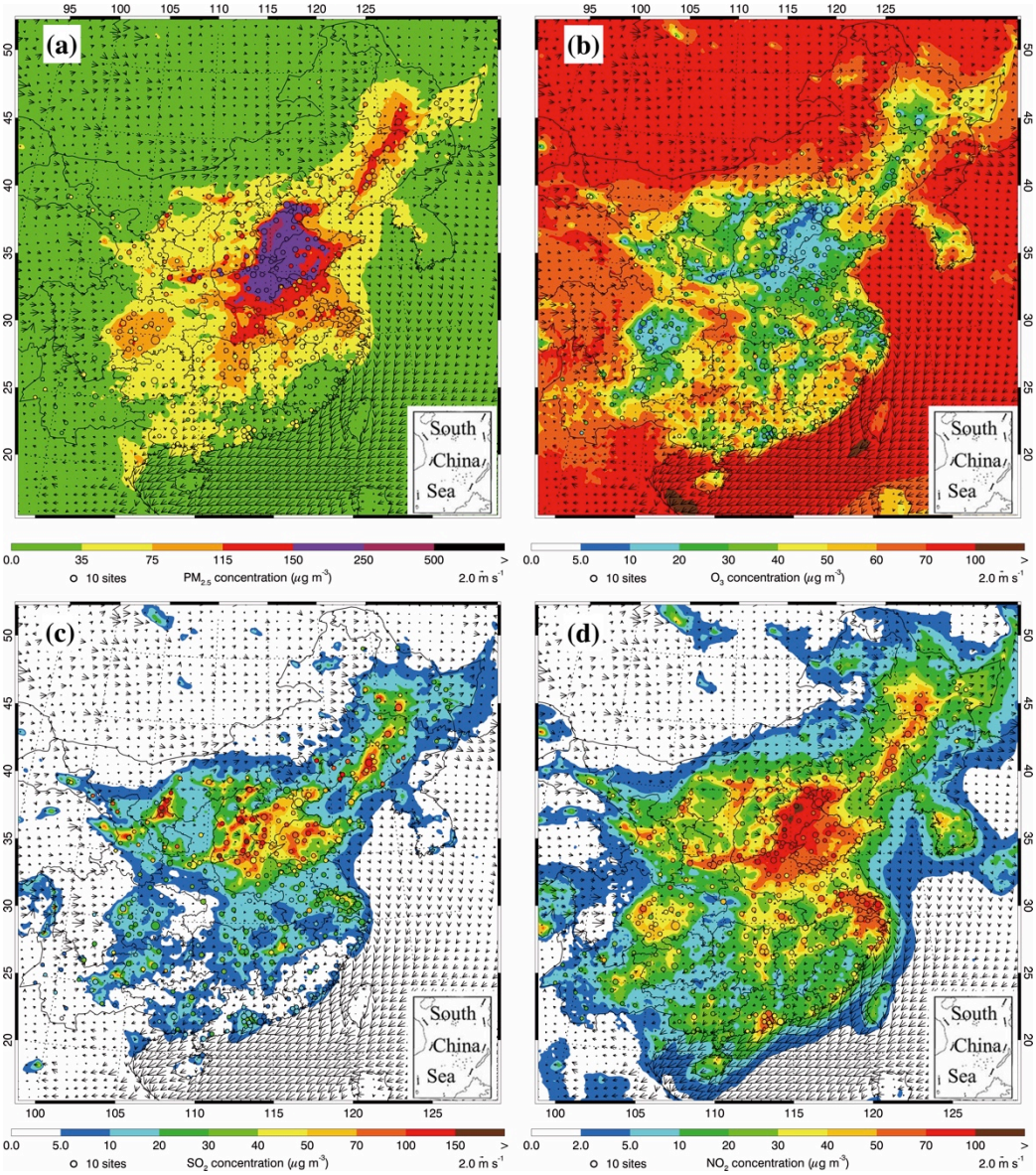

Fig. S3. Pattern comparisons of simulated (color counters) vs. observed (colored circles) near-surface mass concentrations of (a) $PM_{2.5}$, (b) O_3, (c) NO_2, and (d) SO_2 averaged from 05 December 2015 to 04 January 2016. The black arrows indicate simulated surface winds.

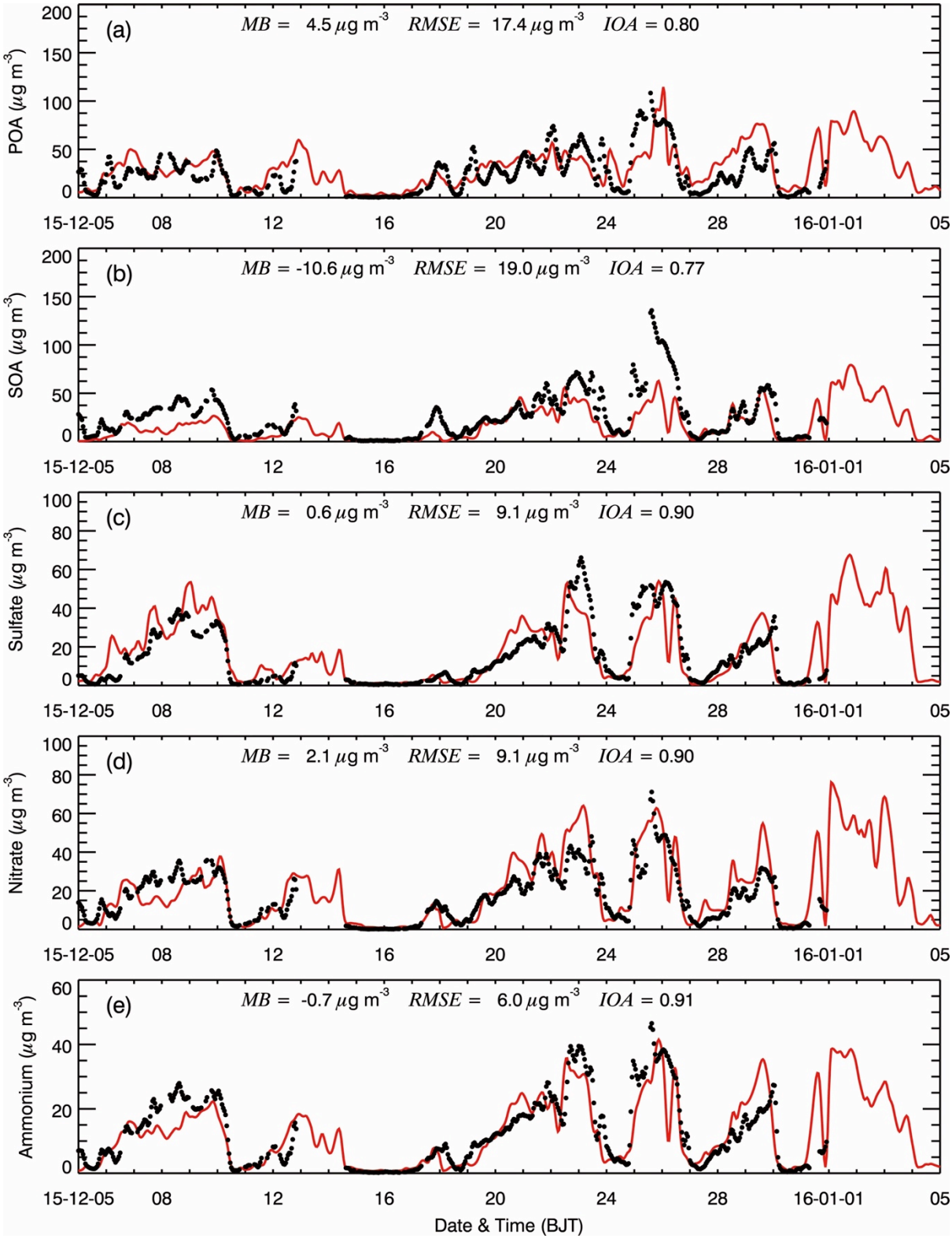

Fig. S4. Comparison of measured (black dots) and simulated (black line) diurnal profiles of submicron aerosol species of (a) POA, (b) SOA, (c) sulfate, (d) nitrate, and (e) ammonium at NCNST site in Beijing from 05 December 2015 to 04 January 2016.

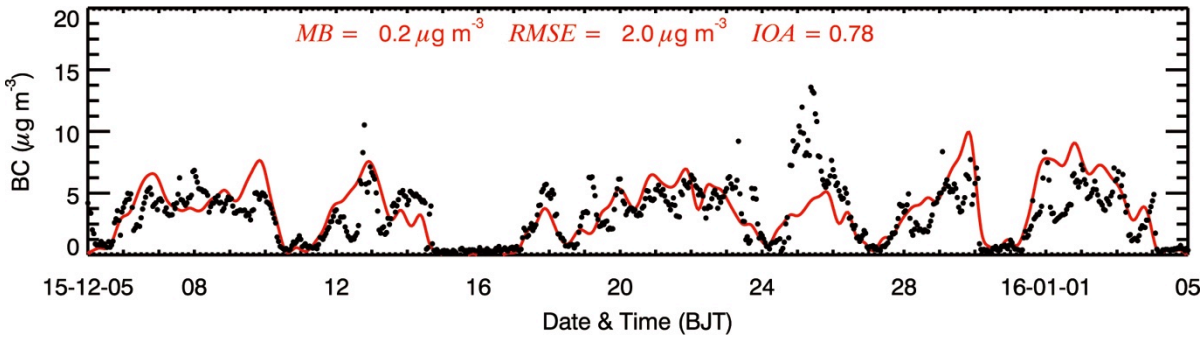

Fig. S5. Comparison of measured (black dots) and simulated (red line) diurnal profiles of BC concentrations at CRAES site in Beijing from 05 December 2015 to 04 January 2016.

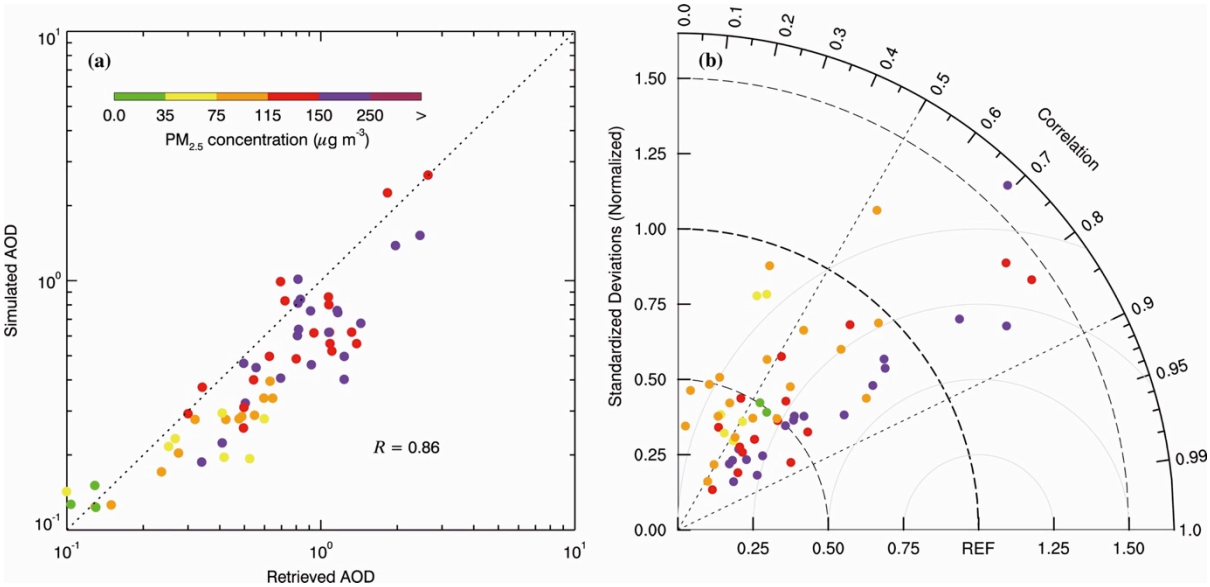

Fig. S6. (a) Scatter plot of the MODIS retrieved and simulated daily AOD at 550nm, (b) Taylor diagram (52) to present the variance, bias and correlation of the retrieved and simulated daily AOD averaged in the NCP from 05 December 2015 to 04 January 2016.

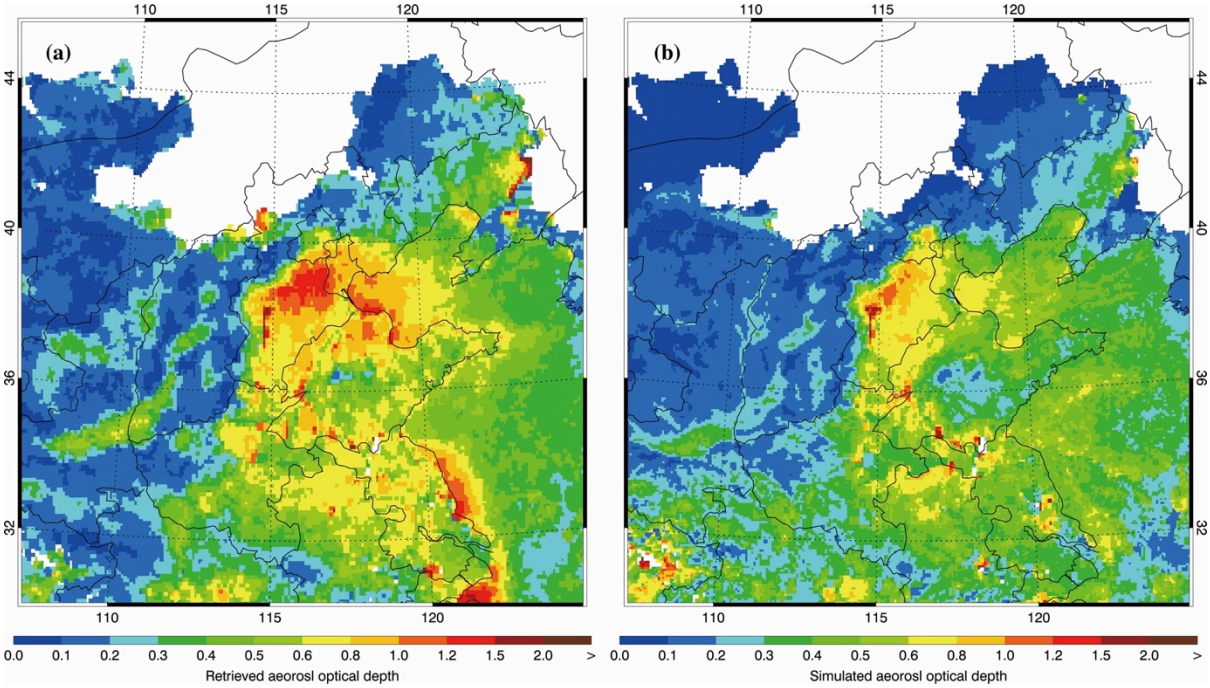

765
766
767 **Fig. S7.** Spatial distribution of (a) retrieved and (b) simulated AOD at 550nm averaged from
768 05 December 2015 to 04 January 2016 in the NCP.
769
770
771
772
773

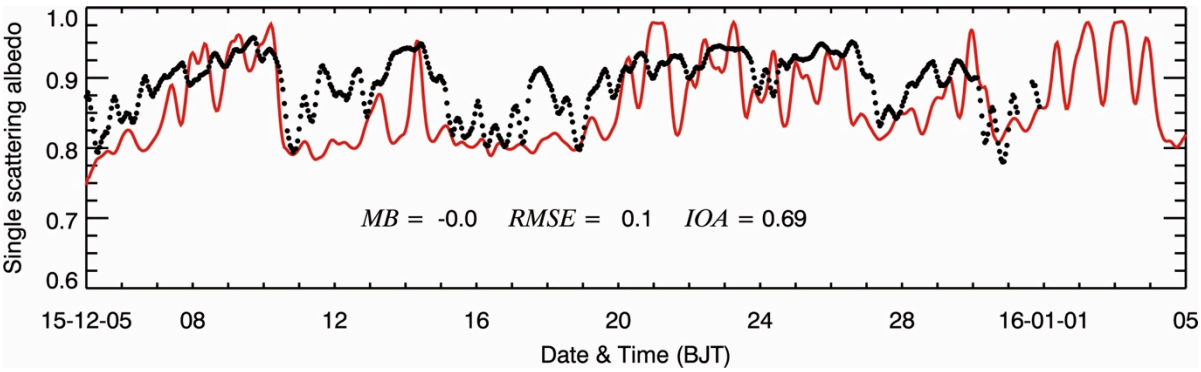

Fig. S8. Comparison of measured (black dots) and predicted (red line) diurnal profiles of SSA at 520nm in Beijing from 05 December 2015 to 04 January 2016.

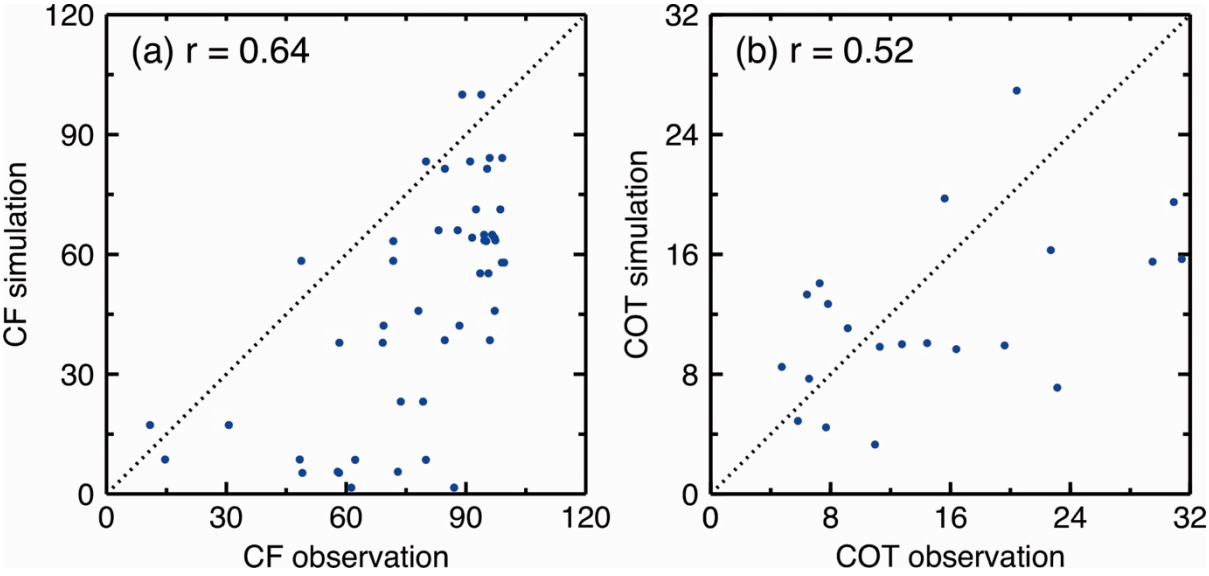

Fig. S9. Scatter plot of the MODIS retrieved and simulated daily (a) cloud fraction and (b) cloud optical thickness averaged in the NCP from 05 December 2015 to 31 December 2015.

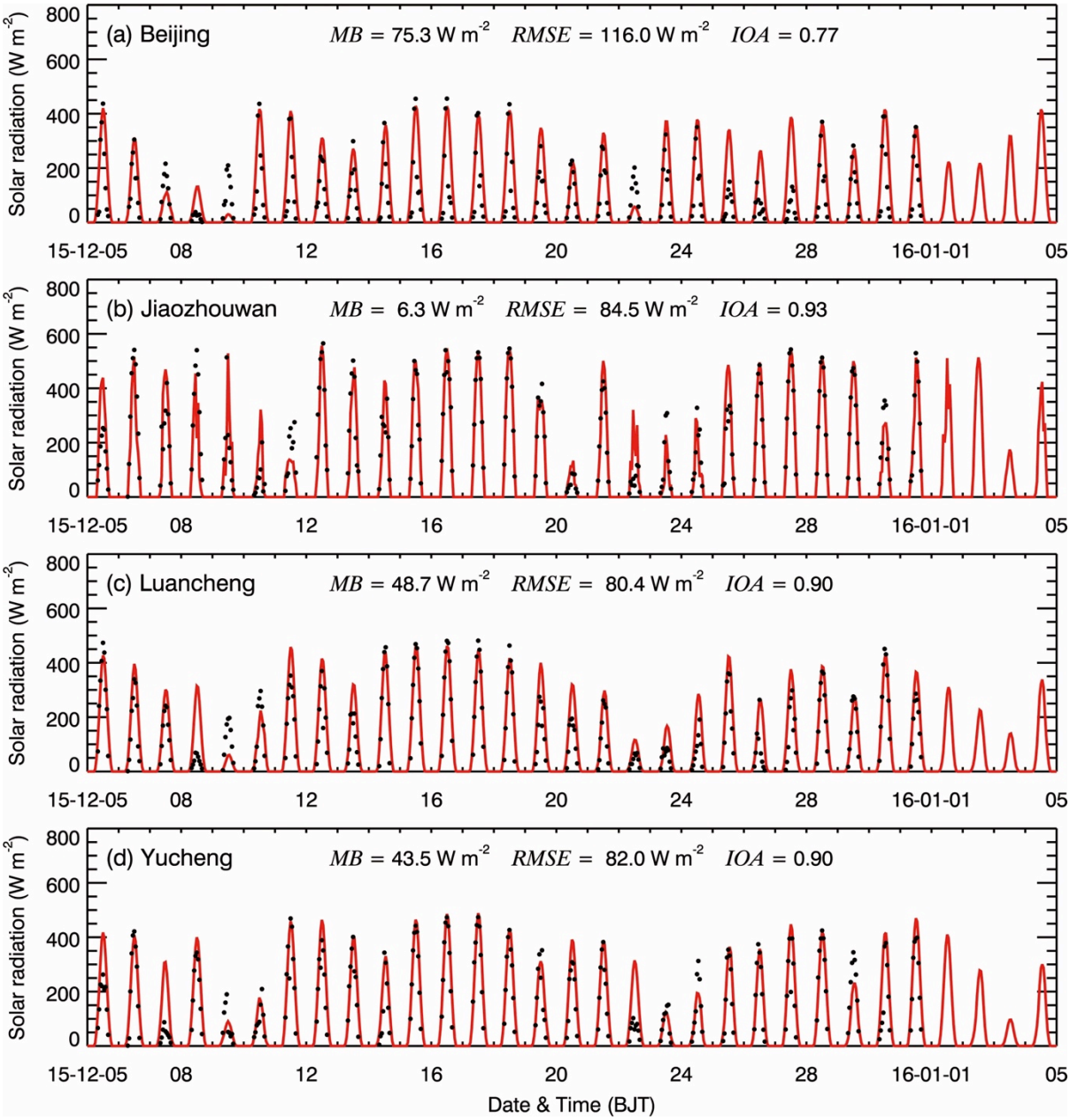

Fig. S10. Comparison of measured (black dots) and predicted (red line) diurnal profiles of the SWDOWN reaching the ground surface in (a) Beijing, (b) Jiaozhouwan, (c) Luancheng, and (d) Yucheng from 05 December 2015 to 04 January 2016.

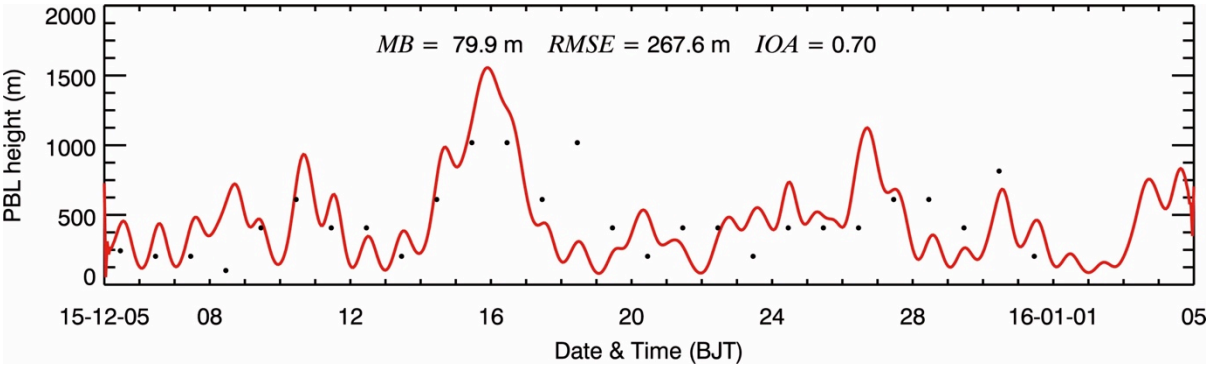

Fig. S11. Comparison of predicted diurnal profile (red line) of PBLH from 05 December 2015 to 04 January 2016 with observations at 12:00 BJT in Beijing.

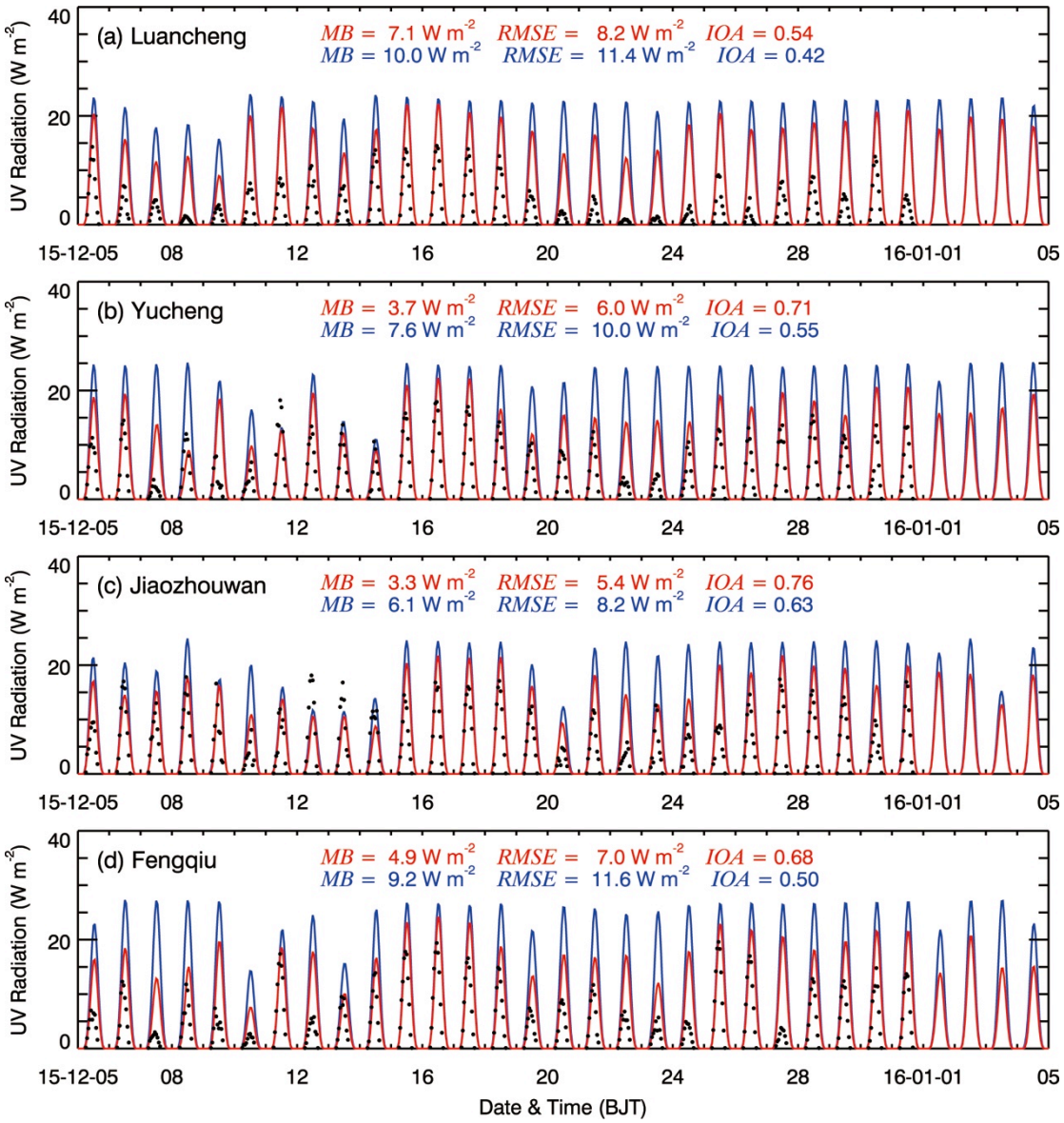

Fig. S12. Comparison of measured (black dots) and predicted diurnal profiles of the ultraviolet radiation in F_BASE (red line) and F_TOT0 (blue line) in (a) Luancheng, (b) Yucheng, (c) Jiaozhouwan, and (d) Fengqiu from 05 December 2015 to 04 January 2016.

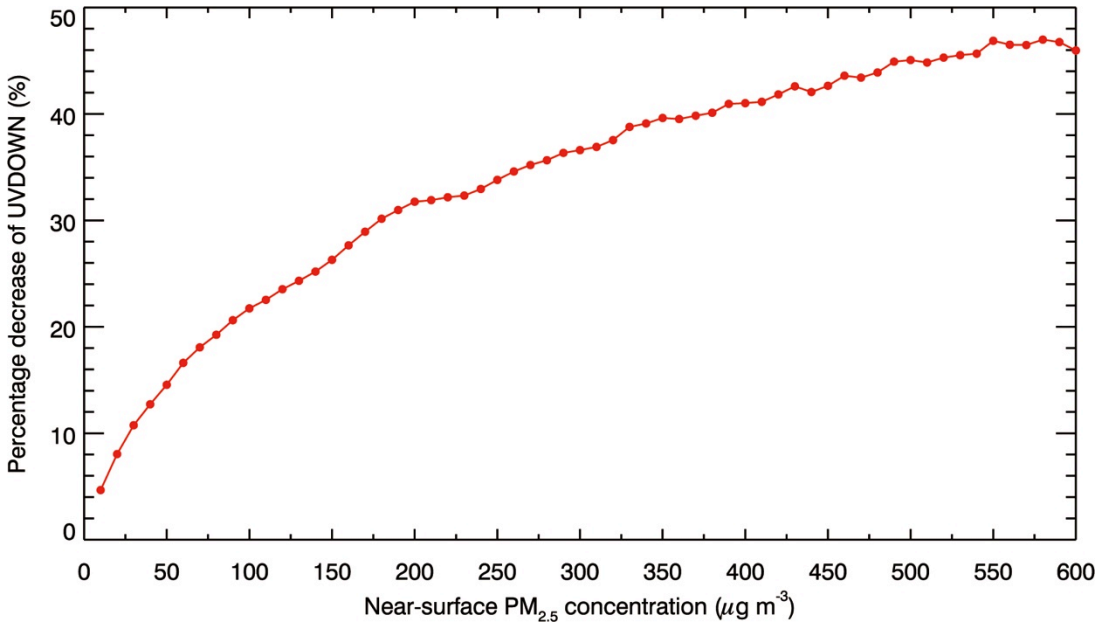

Fig. S13. Average percentage decrease of daytime UVDOWN caused by API as a function of near-surface [$PM_{2.5}$] in the NCP from 05 December 2015 to 04 January 2016.

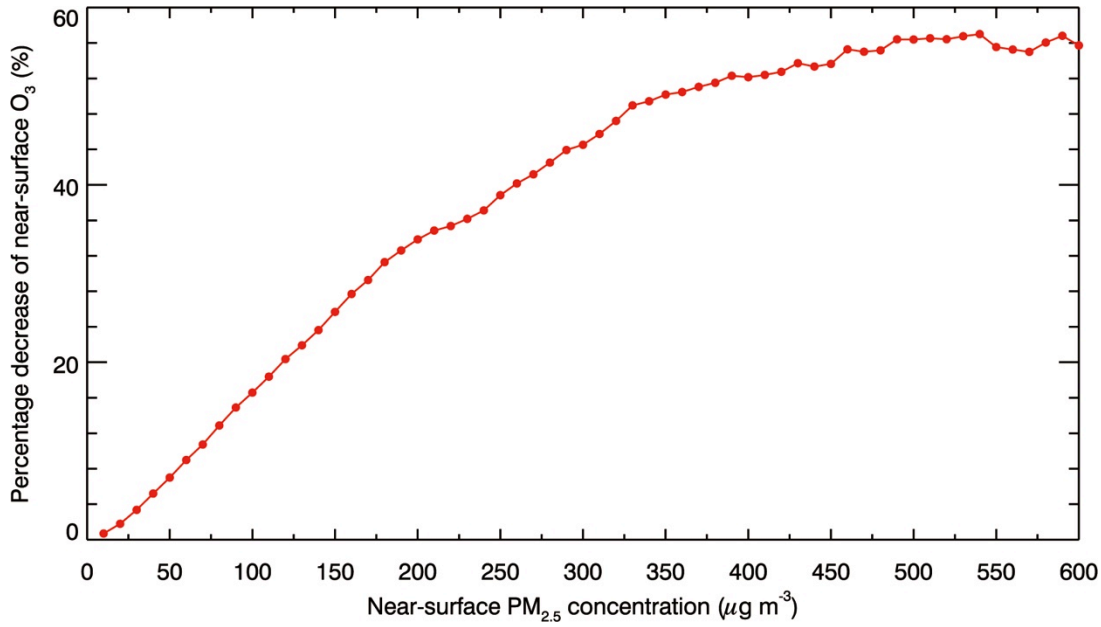

Fig. S14. Average percentage decrease of daytime near-surface O_3 concentration caused by API as a function of near-surface [$PM_{2.5}$] in the NCP from 05 December 2015 to 04 January 2016.

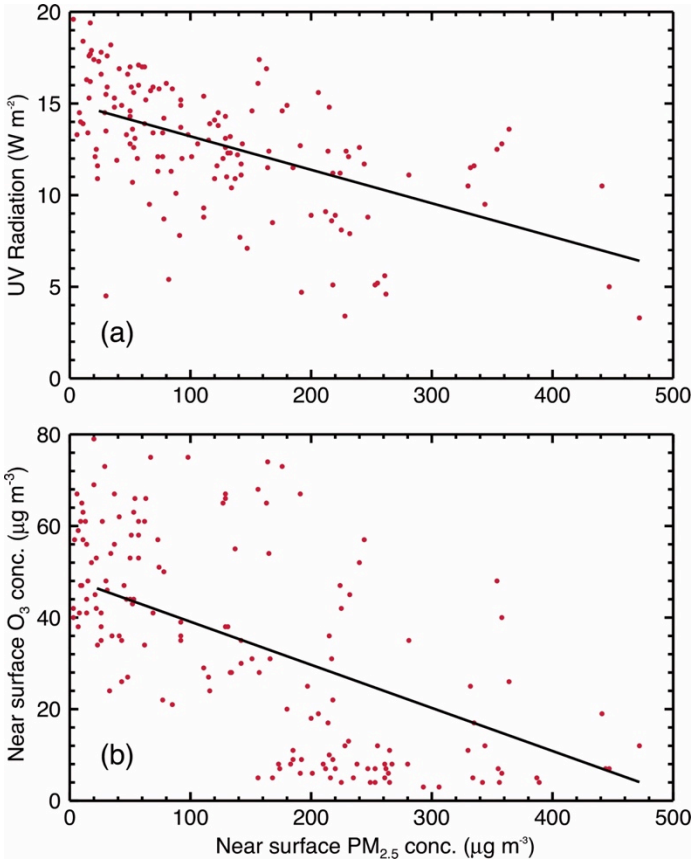

Fig. S15. Scatter plot of (a) the observed UVDOWN and near-surface $PM_{2.5}$ concentrations and (b) near-surface O_3 and $PM_{2.5}$ concentrations in Beijing, Fengqiu, Luancheng, Yucheng, and Jiaozhouwan during noontime (11:00-13:00 BJT) under cloudless days selected from 05 December 2015 to 04 January 2016. The black line indicates the fitted trend line.

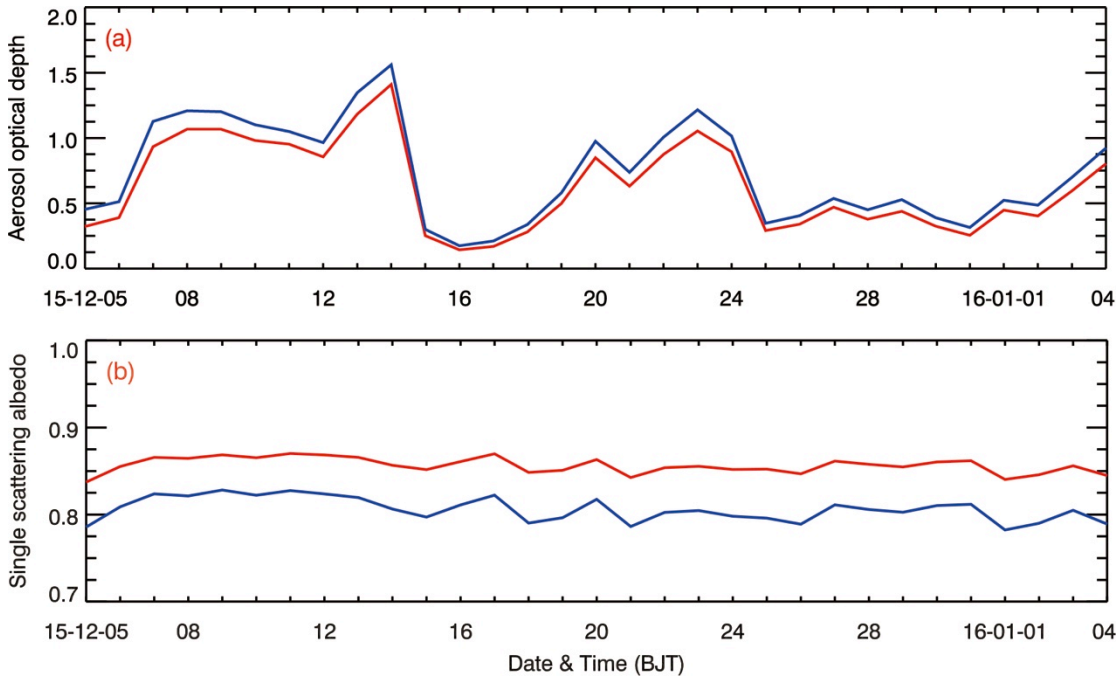

Fig. S16. Daily variations of average daytime AOD and near-surface SSA at 550nm (red line) and 380nm (blue line) layer in the NCP from 05 December 2015 to 04 January 2016.

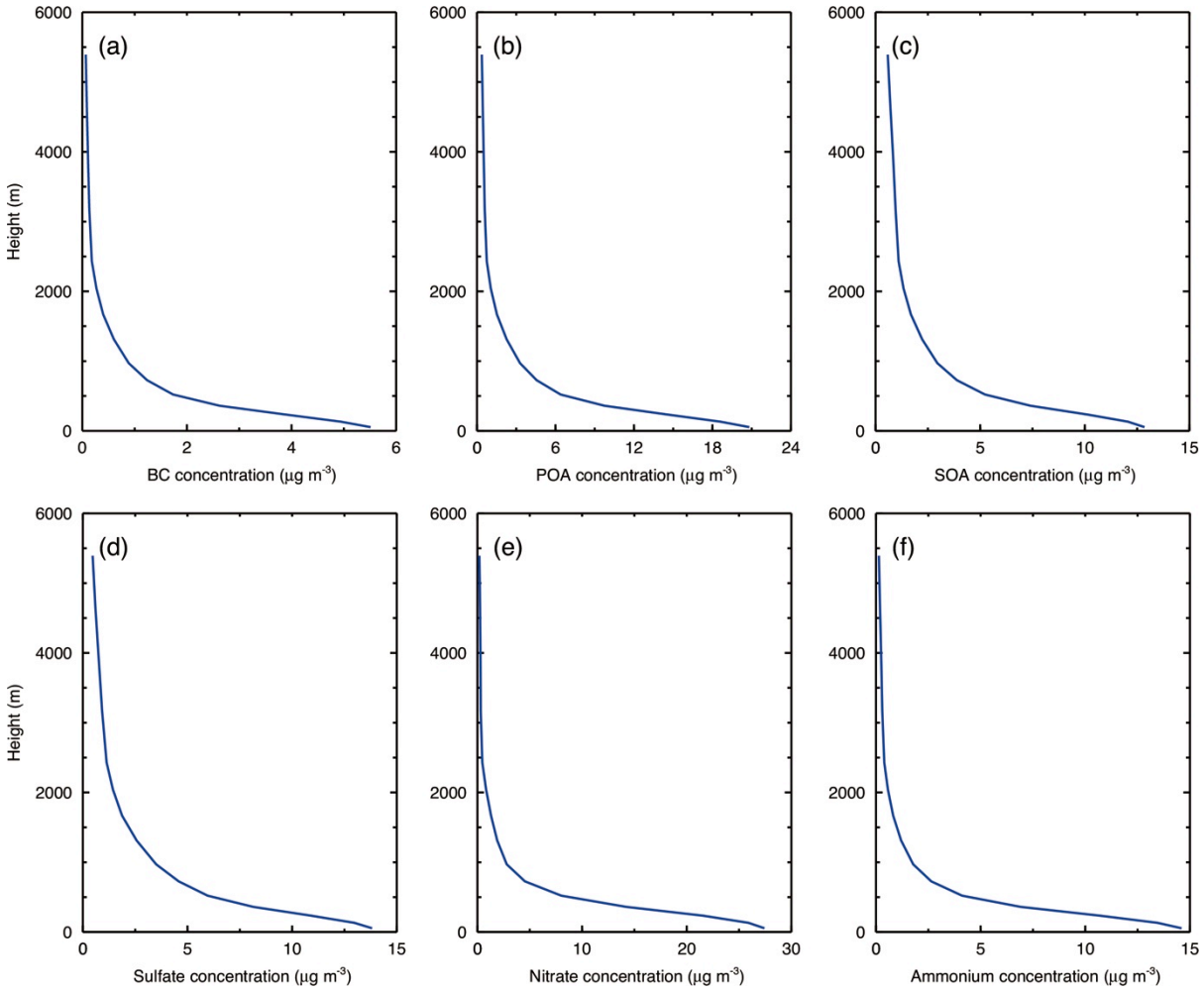

Fig. S17. Vertical profiles of average (a) BC, (b) POA, (c) SOA, (d) sulfate, (e) nitrate, and (f) ammonium in the NCP from 05 December 2015 to 04 January 2016.

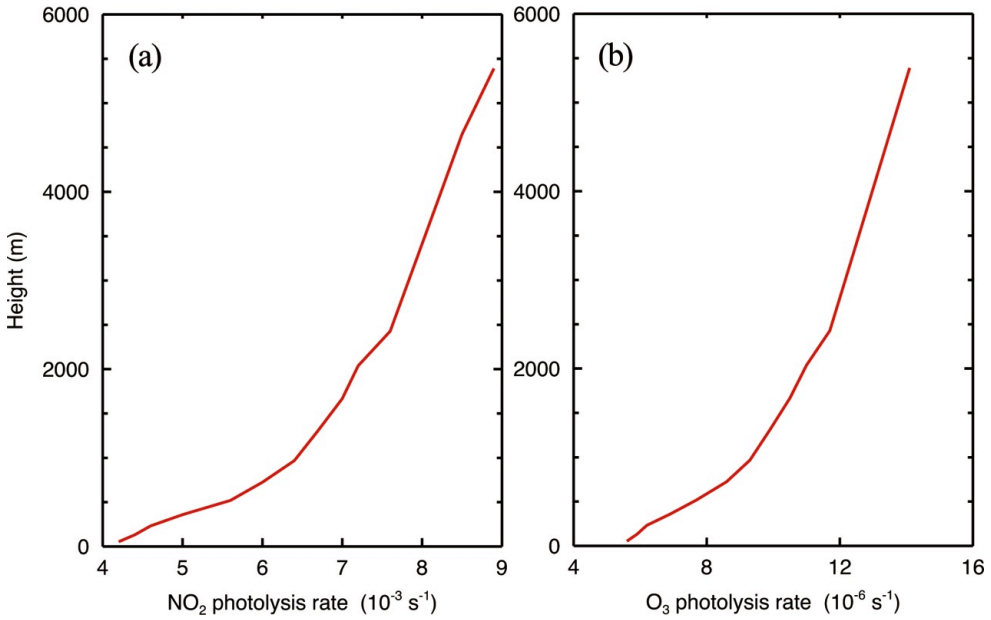

Fig. S18. Vertical profile of average noontime NO_2 and O_3 to O^{1D} photolysis rate in the NCP from 05 December 2015 to 04 January 2016.

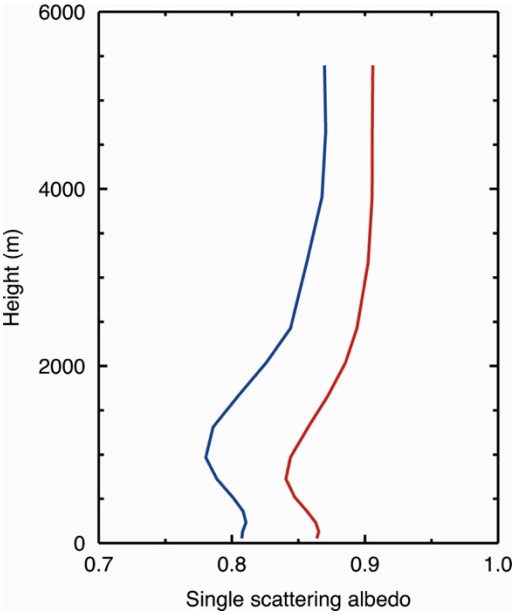

878
879
880 **Fig. S19.** Vertical profiles of average daytime SSA at 550nm (red line) and 380 nm (blue line)
881 in the NCP from 05 December 2015 to 04 January 2016.
882
883
884
885
886

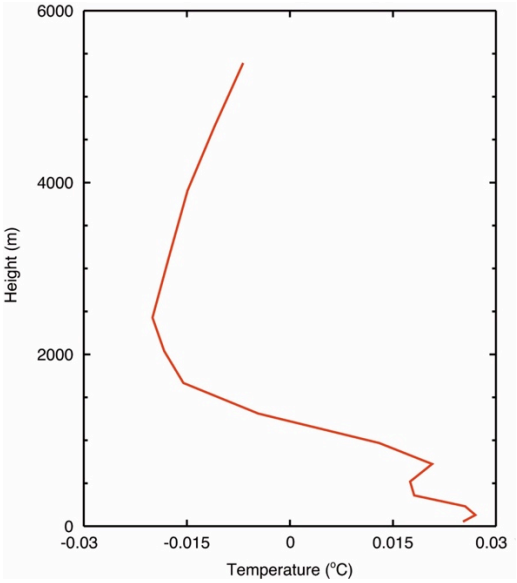

Fig. S20. Vertical profiles of average temperature perturbation caused by API in the NCP from 05 December 2015 to 04 January 2016.

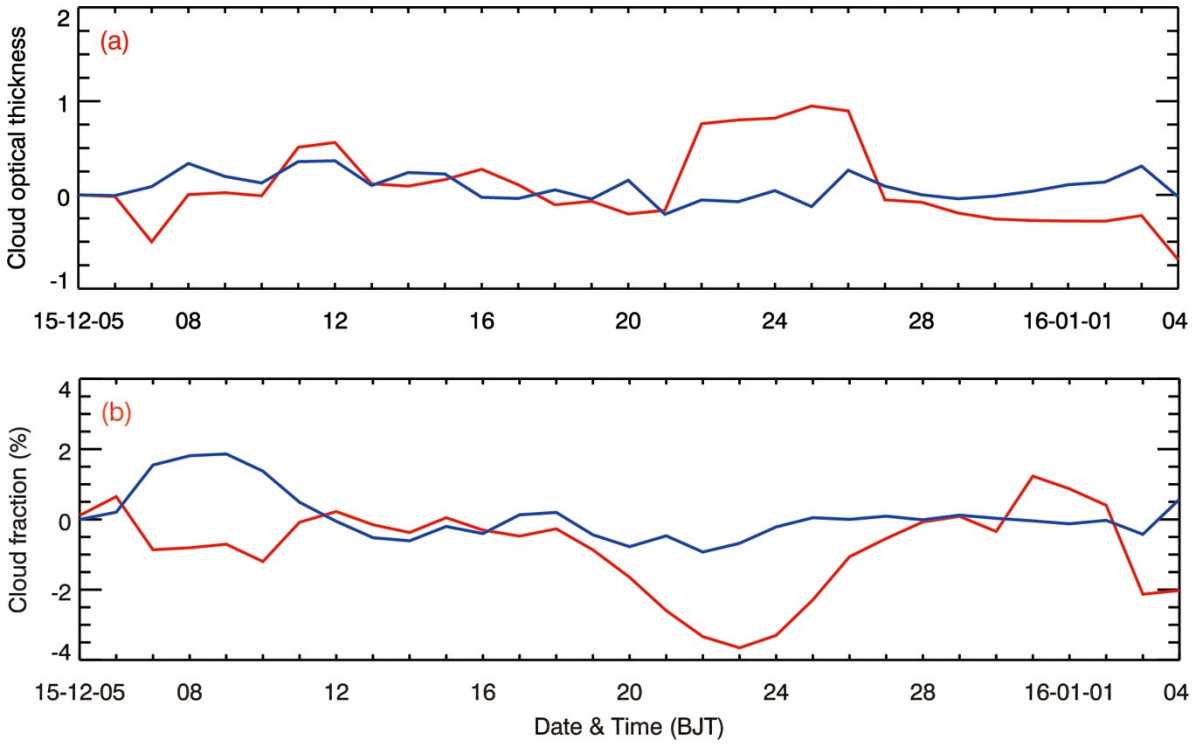

Fig. S21. Daily profiles of variation of average daytime COT and CF caused by ARI (red line) and API (blue line) in the NCP from 05 December 2015 to 04 January 2016.

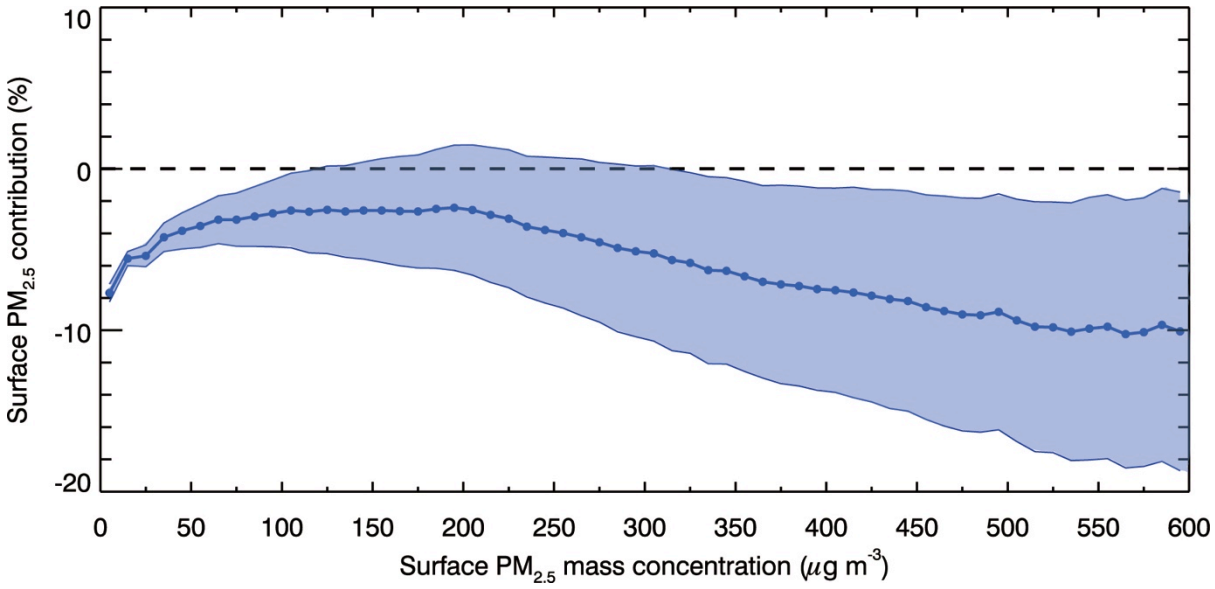

905
906
907 **Fig. S22.** Average percentage contribution of near-surface [$PM_{2.5}$] caused by API (blue line)
908 and error shadow as a function of near-surface [$PM_{2.5}$] in the NCP from 05 December 2015 to
909 04 January 2016.
910
911
912
913
914

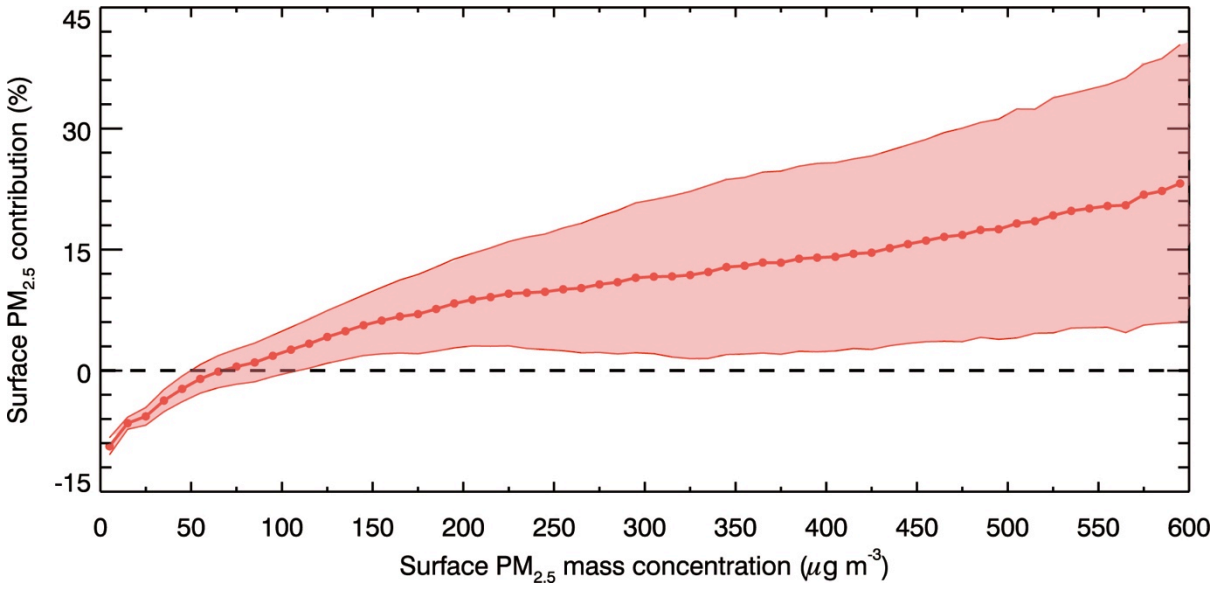

Fig. S23. Average percentage contribution of near-surface [$PM_{2.5}$] caused by ARI (red line) and error shadow as a function of the near-surface [$PM_{2.5}$] in the NCP from 05 December 2015 to 04 January 2016.

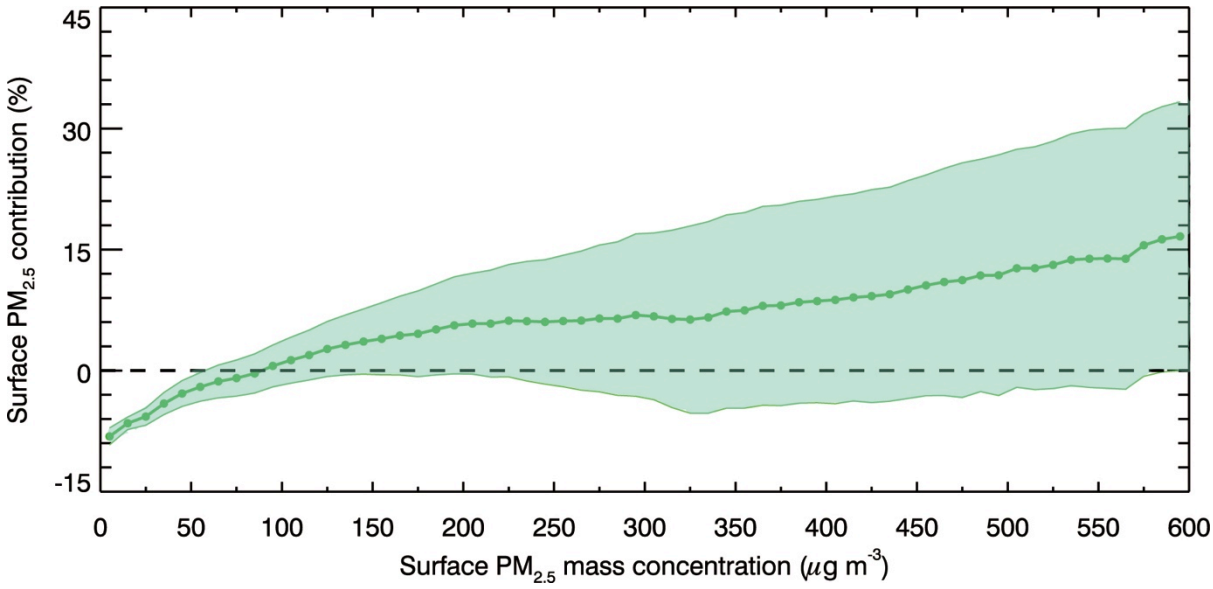

925
926
927 **Fig. S24.** Average percentage contribution of near-surface [$PM_{2.5}$] caused by both API and
928 ARI (green line) and error shadow as a function of near-surface [$PM_{2.5}$] in the NCP from 05
929 December 2015 to 04 January 2016.
930
931
932
933